Astron. Astrophys. 226, 162–182 (1989)

ASTRONOMY AND ASTROPHYSICS

Unified NLTE model atmospheres including spherical extension and stellar winds: method and first results

R. Gabler, A. Gabler, R.P. Kudritzki, J. Puls, and A. Pauldrach

Institut für Astronomie und Astrophysik, Scheinerstrasse 1, D-8000 München 80, Federal Republic of Germany

Received August 17, 1988; accepted April 5, 1989

Summary. NLTE model atmospheres for hot stars that avoid the artificial division between hydrostatic photosphere and supersonic stellar wind envelope are presented. The models are spherically extended and use the density and velocity stratification of radiation driven winds in the entire sub- and supersonic atmosphere. The models need only stellar effective temperature, gravity and radius defined at the inner atmospheric boundary as free parameters and are in principle self-consistent. They yield stellar energy distributions and hydrogen and helium line spectra. First calculations for the O4f star ζ Puppis and a sequence of models for Central Stars of Planetary Nebulae are presented. The results are:

1. The typical Stark broadened lines, normally used for the quantitative spectral analysis of O stars by means of plane-parallel hydrostatic NLTE models (Hγ, Hδ, He II 4542, 4200) are partially affected by sphericity and winds. This will have systematic consequences for the gravity determination in the case of O stars with dense winds, such as Of stars.

2. Hα, Pα, Bα, He II $\lambda\lambda$ 1640, 4686, 10 124 are strongly contaminated by wind emission as observed. For Central Stars Hα and He II 4686 are very promising indicators for stellar mass and radius.

3. The optical to UV energy distribution remains unchanged except for Central Stars close to the Eddington limit.

4. The observed infrared excess is reproduced.

5. The emergent flux shortward of the He II-edge at 228 Å is increased by a factor of a thousand relative to plane-parallel models. This is caused by the presence of the wind outflow in the region where this continuum is formed. This effect is highly important for the ionization of surrounding interstellar gas and might be a very promising way to solve the long-standing problem of the "Zanstra discrepancy" for Central Stars.

Key words: model atmospheres – hot stars – NLTE – stellar winds

1. Introduction

Following the development of detailed NLTE model atmospheres and line formation calculations during the past decade it was possible to fit in detail the observed optical hydrogen and helium line spectra of hot stars for the first time (Auer and Mihalas, 1972). In this way reliable stellar parameters were determined for massive O stars, hot subdwarfs and Central stars of Planetary Nebulae (for recent reviews see Kudritzki and Hummer, 1986; Kudritzki, 1988; Kudritzki and Méndez, 1988). However, with increasing quality of the observational data it became evident that clear discrepancies in some cases still existed. While part of these discrepancies could be resolved by improving the physical details of the line formation calculations (see Herrero, 1987a, b), remainder proved to be significant. Typical examples are the occurrence of He II 4686 and Hα in emission for objects close to the Eddington limit (see for instance Kudritzki et al., 1983; Méndez et al., 1988; Kudritzki and Méndez, 1988). Even for O stars on the main sequence, where these lines go over into absorption, a significant discrepancy with the NLTE calculations remains indicating that He II 4686 and Hα are partially filled with emission (see Kudritzki, 1980; Simon et al., 1983).

The usual explanation for this discrepancy, also used in the papers just cited, is that the emission in these lines originates in the surrounding stellar winds. Several detailed line formation calculations have been performed, which indeed show that the expanding wind envelope provides enough emission measure to produce this effect (Cassinelli et al., 1978; Klein and Castor, 1978; Olson and Ebbetts, 1981). In addition, Leitherer (1988) recently developed scaling relations for the Hα wind emission luminosity (on the basis of Klein and Castor's work) as a function of mass-loss rate, which when applied to the massive O stars yield mass-loss rates roughly in agreement with values obtained by other methods. Thus, the concept of additional wind emission contaminating the photospheric radiation is certainly promising. However, the procedure used to calculate this wind emission up to now has a crucial limitation that becomes important as soon as quantitative comparisons with the observations are intended.

It makes an artificial division between the hydrostatic photosphere and the supersonically expanding stellar wind. This has several important consequences: First, the location of the borderline between these two regions has to be defined as a free parameter. Normally either a "photospheric outflow velocity" v_0 is adopted, that fixes the density ρ_0 at this boundary via the equation of continuity, or the radius of the sonic point r_s is fixed from an ad hoc velocity law that again yields ρ_0 in the same way. As test calculations not only for Hα and He II 4686 but also for the near and far IR continuum show, this free parameter strongly

Send offprint requests to: R. Gabler

influences the amount of (central) line emission and IR continuum shape. Second, the radiative interaction between photosphere and wind needs to be specified. Normally, the emergent flux of the plane-parallel NLTE models without winds is simply taken as the inner radiative boundary of the wind region. Apart from the important effect of wind blanketing for the photospheres (see Abbott and Hummer, 1985) this procedure is most probably correct for the continuous radiation field of O stars between 228 Å and 10000 Å. However, shortward of 228 Å (the He II-edge) the continuum becomes optically thin only far out in the stellar wind. This has crucial consequences for the He II line formation problem and the line formation of ions with ionization edges in that spectral region (Pauldrach, 1987a, b; Pauldrach and Herrero, 1988). Simple "on the spot" or "escape probability" approximations for the formation of this continuum lead to spurious results compared with the solution of the exact radiative transfer problem of this case.

Of course, the line cores are also not optically thin at this artificial boundary between photosphere and wind. Thus, the normal procedure of taking the line profiles of the photospheric NLTE models as inner boundary condition for the wind radiative transfer or, even worse, just simply adding them to the wind emission or ignoring the photospheric line radiation completely, is consequently questionable. All the wind emission profiles of H and He II published so far suffer from this approximate treatment. This is particularly important for lines like Hγ, Hβ, He II 4542, 5412, whose profiles are normally used for the precise determination of stellar parameters by fitting with profiles of hydrostatic, plane-parallel NLTE models (see Kudritzki, 1980; Kudritzki et al., 1983; Simon et al., 1983; Bohannan et al., 1986). To investigate whether the observed wind profiles of these lines are weakly wind-contaminated or not, which would have consequences for the determination of the stellar parameters, is not possible in this simple way.

Also, purely from the theoretical standpoint the artificial division between wind and photosphere is unsatisfactory because it introduces additional free parameters. What is needed is a self-consistent theory in which only the necessary stellar parameters are used. In the case of plane-parallel atmospheres these parameters are effective temperature $T_{\rm eff}$, gravity $\log g$ and chemical composition. In the case of spherically extended atmospheres one has to specify in addition the stellar radius at which $T_{\rm eff}$ and $\log g$ are given. For a reliable model atmosphere theory these parameters must be sufficient to predict the energy distribution, line profiles, terminal velocity v_∞ and mass-loss rate.

In this paper we present a first step towards the development of such a theory. The idea is simple: We combine our radiation driven stellar wind code (Pauldrach et al., 1986; Pauldrach, 1987b; Puls, 1987b), which yields the density structure and velocity field in the entire (sub- and supersonic) atmosphere as a function of the three stellar parameters, with a new NLTE model atmosphere code for spherical geometry comparable to those developed by Mihalas and Hummer (1974) and Gruschinske and Kudritzki (1979) which in addition gives the temperature structure. In this way, "unified model atmospheres" are obtained free from unnecessary parameters.

We will discuss the details of the method including the remaining inconsistencies in Sect. 2. In Sect. 3 we will present first results for the O4f star ζ Puppis as a representative of massive O stars. In Sect. 4 a sequence of models is calculated for Central Stars of Planetary Nebulae. These represent a case of larger photospheric extension and exhibit an interesting systematic behaviour in the line emission. In the final Sect. 5 we will discuss the important steps for future work.

2. Method

2.1. The stellar parameters

The principal input parameters for our models are specified at a fixed Thomson optical depth in the atmosphere:

$$T_{\rm eff}^{*} = T_{\rm eff}\,(\tau_{\rm Th} = \tau_{*})$$
$$g_{*} = g\,(\tau_{\rm Th} = \tau_{*})$$
$$R_{*} = R\,(\tau_{\rm Th} = \tau_{*}) \qquad (1)$$

τ_{*} is normally chosen to be the Thomson optical depth at the inner boundary of the atmosphere. A value large enough (of the order of ten to forty) is adopted to assure that the continuous radiation is thermalized at all wavelengths at this depth and that the changes in $T_{\rm eff}$, g_{*}, R_{*} are small, if τ_{*} is varied. The corresponding Rosseland optical depth $\tau_{\rm Ross}\,(\tau_{*})$ is then larger than 100 in all cases.

2.2. Density and velocity stratification

With the stellar parameters defined by Eq. (1) the theory of radiation driven winds as recently extended by Pauldrach et al. (1986, hereinafter PPK) yields the mass-loss rate $\dot{M}$, density structure $\rho(r)$ and the velocity field $v(r)$. The stellar wind code does not include the energy balance constraint. Thus a prespecified temperature stratification $T(r)$ must be chosen as input at this stage. PPK have shown that the resulting density and velocity structure does not depend on the detailed choice of $T(r)$ as long as the force multiplier parameters k, α, δ (see PPK) are fixed. Thus, for simplicity, $T(r) = T_{\rm eff}$ is adopted in the region where $v(r)/v_{\rm s} \geq 0.1$ in this first step. In deeper layers a grey solution (see PPK) is adopted.

The force multiplier parameters k, α, δ are in principle not free. They have to be computed as a function of the stellar parameters from the strengths of 250000 metal lines contributing to the line force (Abbott, 1982). Such computations can be done either using approximate NLTE for metal occupation numbers in the wind (Abbott, 1982; Kudritzki et al., 1987) or detailed self-consistent NLTE calculations (Pauldrach, 1987a) perhaps even including multi-line effects (Puls, 1987a). A problem arises because k, α, δ do depend slightly on the pre-specified temperature structure $T(r)$. Thus, for a fully self-consistent treatment an iteration of the computation of k, α, δ and then of $\rho(r)$ and $v(r)$ is needed with $T(r)$ coming from the NLTE model atmosphere calculation (see below). However, at present, where only the hydrogen and helium opacities are taken into account for the radiative equilibrium of the NLTE models, the resulting effects are small (see Pauldrach, 1987a, b; Puls 1987a, b). Therefore, for the results presented in this paper, k, α, δ have not been iterated. In future work, where the bound-bound and bound-free opacity of the most important metals will have to be included in the radiative equilibrium, this iteration cycle might be necessary.

2.3. NLTE temperature structure

The temperature structure is calculated using a new NLTE model atmosphere code for spherically extended atmospheres. In principle very similar input physics to that of Mihalas and Hummer

(1974) and Gruschinske and Kudritzki (1979) is adopted, except that the hydrostatic equation is removed and replaced by $\rho(r)$ computed from the stellar wind code. Moreover, the velocity field $v(r)$ is of course taken into account in the bound-bound radiative rates. The equation, that yields $T(r)$ is the radiative equilibrium constraint

$$\int_0^\infty (\chi_\nu J_\nu - \eta_\nu)\, d\nu = 0, \tag{2}$$

where χ_ν and η_ν are the absorption and emission coefficients, respectively, and J_ν is the angle averaged mean intensity. As already mentioned, only hydrogen and helium opacity (bound-bound, bound-free, free-free) and Thomson scattering are taken into account at the moment. This needs a detailed justification:

The main argument is of course that hydrogen and helium are the major sources of opacity in the atmospheres of hot stars with respect to radiative equilibrium. The standard plane-parallel hydrostatic NLTE-models, used for quantitative spectroscopy also include only hydrogen and helium (Auer and Mihalas, 1972; Kudritzki, 1973, 1976; Clegg and Middlemass, 1987). The effects of C, N, O NLTE bound-free opacity on the temperature structure have been studied by Mihalas (1972) and Husfeld et al. (1984) and found to be moderate. Anderson (1985) has included the detailed NLTE line opacity of C III, C IV, C V for the special case of a model with $T_{\rm eff} = 35\,000$ K and $\log g = 4.0$ and found a substantial temperature drop in the outer atmospheric layers caused by the C IV resonance lines. However, this drop occurs, where the continuum and all of the hydrogen lines as well as the helium lines in the optical spectrum have formed already so that they are only marginally affected (see also the discussion by Kudritzki and Hummer (1986)). Werner (1987, 1988) has calculated a small grid of models for very hot subdwarfs including the NLTE line opacity of some hundred lines of carbon (plus hydrogen and helium). His results show that the effects on the hydrogen and helium lines and the continuum are small although not completely negligible for precise quantitative work. Since the main objective of this paper is to investigate the importance of the wind contamination of the hydrogen and helium lines and the continuum, it is reasonable to use the same opacities as the standard hydrostatic models and to estimate the wind effects from a differential comparison.

It is of course clear that in future work the opacity of the metals has to be taken into account for the radiative equilibrium as has already been done for the equation of motion and the computation of the line force (see Pauldrach, 1987a, b; Puls, 1987a, b). This necessary extension of the work presented here is presently under way. The importance of the metals for the radiative energy balance in the wind is clearly indicated by the extensive calculations of Drew (1988), who however also introduced the concept of an artificial division between photosphere and wind and used an inadequate approximation in treating the continuous radiative transfer. In addition, the ionization equilibrium calculations for the metals by Drew are still very approximate in the treatment of excited levels, because collisional excitation is neglected. On the other hand, it is clear that the effects of the metal line opacity will become important for densities below 10^{-13} g cm^{-3}, because then usual recombination theory becomes applicable and forbidden line cooling becomes important.

As for the hydrostatic models, 5 NLTE levels of H and He I and 10 NLTE levels of He II are taken into account for the bound-free opacity. The bound-bound opacity results from all lines connecting these levels. The occupation numbers are obtained from the solution of the corresponding rate equations, where additional upper levels are taken into account in LTE for the particle conservation (11 for H and He I, 22 for He II). The major difference from the hydrostatic code lies in the treatment of the line transitions since they are affected by the presence of the velocity field in our case. The ideal choice would be to formulate the radiative line transfer in the comoving frame, which would assure a correct physical treatment in the subsonic region as well. On the other hand, from our experience with the hydrostatic codes this is the region where the line cores are already optically thick and the rate equations are dominated by the continuum transitions. Thus, we have chosen a simpler procedure which appears to be accurate enough for the determination of the temperature structure: We use the Sobolev approximation for the line transfer, which is appropriate in the supersonic region where the line cores are normally formed. In the subsonic region the escape probabilities are then small enough so that the line radiative rates become unimportant compared with other transition mechanisms and the continuum transitions dominate as in the hydrostatic case. After the temperature structure has been determined in this way, we perform subsequent line formation calculations on a fixed temperature structure in the comoving frame to have the correct radiative transfer and to check the approximate procedure. Thus our final rate equations read

$$\begin{aligned} & n_i\left(\sum_{j>i}(I_c\beta_c B_{ij}+C_{ij})+\sum_{j<i}(\beta A_{ij}+I_c\beta_c B_{ij}+C_{ij})\right)+n_i(R_{iK}+C_{iK}) \\ & -\sum_{j>i} n_j(\beta A_{ji}+I_c\beta_c B_{ji}+C_{ji})-\sum_{j<i} n_j(I_c\beta_c B_{ji}+C_{ji}) \\ & -n_+(R_{Ki}+C_{Ki})=0 \end{aligned} \tag{3}$$

where β_c, β are the escape probabilities and I_c is the core intensity of the corresponding transition in the Sobolev theory. A_{ij}, B_{ij} are the Einstein transition probabilities and C_{ij} the collision rates (computed as in Kudritzki, 1976; Kudritzki and Simon, 1978). The bound-free radiative rates R_{iK} and R_{Ki} are calculated within the formalism of accelerated lambda iteration (Werner and Husfeld, 1985, hereinafter ALI) taking into account the recent modification by Pauldrach and Herrero (1988). The monochromatic mean intensity of the continuum transition in the $l^{\rm th}$ ALI-interaction is then written as (the frequency index is k).

$$J_k^l = J_k^{l-1} + \Lambda^*(S_k^l - S_k^{l-1}). \tag{4}$$

The 'Lambda-Operator' Λ^* applied to the difference of two consecutive source functions S_k drives the convergent behavior of our mean intensity J_k. The choice of Λ^* is free and we have used both the formulation of Hamann (1986) and of Olson, Auer, Buchler ("OAB", 1986). The final form of our bound-free radiative rates is then (see Pauldrach and Herrero)

$$\begin{aligned} R_{ki} &= 4\pi\left(\frac{\eta_i}{n_+}\right)^* \sum_k \frac{\sigma_{ik}}{h\nu_k}\frac{2h\nu_k^3}{c^2}\exp\left(-\frac{h\nu_k}{kT}\right)\Lambda^*\left(\frac{S_k^{l-2}-S_k^{l-1}}{S_k^{l-1}}\right) w_k \\ &\quad + 4\pi\left(\frac{n_i}{n_+}\right)^* \sum_k \frac{\sigma_{ik}}{h\nu_k}\left(J_k^{l-1}+\frac{2h\nu_k^3}{c^2}\right)\exp\left(-\frac{h\nu_k}{kT}\right) w_k \end{aligned} \tag{5}$$

$$R_{ik} = 4\pi \sum_k \frac{\sigma_{ik}}{h\nu_k} J_k^{l-1}\, w_k;$$

w_k are frequency weights and σ_{ik} the absorption cross-sections; $(n_i/n_+)^*$ is the usual LTE occupation ratio. This choice of the radiative rates speeds convergence.

The continuous radiation field for the bound-free and bound-bound rates is obtained by the solution of the depth discretized transfer equation:

$$-\frac{(f_k q_k r^2)^{d-1} J_k^{d-1}}{\Delta\tau_k^{d-\frac{1}{2}} \Delta\tau_k^d} + \frac{(f_k q_k r^2)^d J_k^d}{\Delta\tau_k^d}\left(\frac{1}{\Delta\tau_k^{d+\frac{1}{2}}} + \frac{1}{\Delta\tau_k^{d-\frac{1}{2}}}\right)$$
$$-\frac{(f_k q_k r^2)^{d+1} J_k^{d+1}}{\Delta\tau_k^{d+\frac{1}{2}} \Delta\tau_k^d} + \left(\frac{r^2}{q_k}\right)^d (J_k^d - S_k^d) = 0. \quad (6)$$

d is the depth index and the monochromatic optical depth steps are defined as

$$\Delta\tau_k^{d-\frac{1}{2}} = \tfrac{1}{2}(q_k^{d-1}\omega_k^{d-1} + q_k^d \omega_k^d)(m^d - m^{d-1})$$
$$\Delta\tau_k^{d+\frac{1}{2}} = \tfrac{1}{2}(q_k^d \omega_k^d + q_k^{d+1}\omega_k^{d+1})(m^{d+1} - m^d)$$
$$\Delta\tau_k^d = \tfrac{1}{2}(\Delta\tau_k^{d-\frac{1}{2}} + \Delta\tau_k^{d+\frac{1}{2}}), \quad (7)$$

with $\omega_k^d = \chi_k^d/\rho^d$ being the ratio of opacity over density and m^d the mass in a square centimetre column reaching radially to that depth (see Auer and Mihalas, 1969). J_k^d and S_k^d are mean intensity and source function, respectively. f_k^d is the Eddington factor defined by the zero- and second-order angle moments of intensity

$$f_k^d = \frac{K_k^d}{J_k^d}. \quad (8)$$

The sphericality factor q_k^d was first introduced by Auer (1971) and is calculated by integrating

$$\frac{\mathrm{d}q_k}{\mathrm{d}r} = \frac{q_k}{r}\left(\frac{3f_k - 1}{f_k} - 2\right) \quad (9)$$

in an extra iteration cycle together with f_k^d in the formal solution of the angle dependent transfer equation (see below). The boundary conditions for the radiative transfer are

—at the inner boundary

$$\frac{(f_k q_k r^2)^{\mathrm{ND}} J_k^{\mathrm{ND}} - (f_k q_k r^2)^{\mathrm{ND}-1} J_K^{\mathrm{ND}-1}}{\Delta\tau_k^{\mathrm{ND}-\frac{1}{2}}} + r^{2\mathrm{ND}}(g_k^{\mathrm{in}} J_k^{\mathrm{ND}} - \tfrac{1}{2} B_k^{\mathrm{ND}})$$
$$-\frac{r^{2\mathrm{ND}}}{\chi_k^{\mathrm{ND}}}\frac{\partial B_k}{\partial T}\bigg|_{\mathrm{ND}} \frac{H - \sum_{k'}(\frac{1}{2}B_{k'}^{\mathrm{ND}} - g_{k'}^{\mathrm{in}} J_{k'}^{\mathrm{ND}}) w_{k'}}{\sum_{k'} 1/\chi_{k'}^{\mathrm{ND}} (\partial B_{k'}/\partial T)_{\mathrm{ND}} w_{k'}} = 0 \quad (6a)$$

—and at the outer boundary

$$\frac{(f_k q_k r^2)^2 J_k^2 - (f_k q_k r^2)^1 J_k^1}{\Delta\tau_k^{3/2}} - (g_k^{\mathrm{out}} r^2)^1 J_k^1 - \tfrac{1}{2}(r^2/q_n)^1 (J_k^1 - S_k^1) = 0 \quad (6b)$$

where g_k^{in}, g_k^{out} are the Eddington factors with respect to the first-order angle moments of intensity. B_k designates the Planck-function and S_k is the source-function. H is the frequency integrated flux, given by the effective temperature T_{eff} and the star radius R_*. The frequency sums at the inner boundary condition represent frequency integration.

The discretized Eq. (2) then reads at every depth point

$$\sum_k (\chi_k^{\mathrm{c}} J_k^{\mathrm{c}} - \eta_k^{\mathrm{c}}) w_k$$
$$+ \sum_{\mathrm{l,u}} \frac{h\nu_{\mathrm{ul}}}{4\pi}\left(B_{\mathrm{lu}}\left(n_{\mathrm{l}} - \frac{g_{\mathrm{l}}}{g_{\mathrm{u}}} n_{\mathrm{u}}\right)\beta_{\mathrm{c}} I_{\mathrm{c}} - \beta A_{\mathrm{ul}} n_{\mathrm{u}}\right) = 0 \quad (10)$$

The last term is the contribution of the lines in the Sobolev formulation, whereas the first term refers to the continuum. The symbols are the same as in the rate-equations (g_{l}, g_{u} are statistical weights. The frequency ν_{ul} is the central line frequency). For a discussion of this equation see also Hillier (1987, Appendix).

In Eq. (10) it is also possible to eliminate J_k^{C} in the first term by Eq. (4). Equation (10) then reads

$$\sum_k (\chi_k^{\mathrm{C}}(J_k^{l-1} + \Lambda^*(S_k^l - S_k^{l-1})) - n_k) w_k$$
$$+ \sum_{\mathrm{l,u}} \frac{h\nu_{\mathrm{ul}}}{4\pi}\left(B_{\mathrm{lu}}\left(n_{\mathrm{l}} - \frac{g_{\mathrm{l}}}{g_{\mathrm{u}}} n_{\mathrm{u}}\right)\beta_{\mathrm{c}} I_{\mathrm{c}} - \beta A_{\mathrm{ul}} n_u\right) = 0. \quad (11)$$

For the iterative solution of Eq. (3), (6), (10) or (11) we use two alternative procedures:

i) Complete linearization

Here we linearize Eq. (3), (6), (10) together with the other constraints for charge and particle conservation by a Newton-Raphson expansion and solve for the corrections by a Feautrier elimination (see Mihalas and Auer, 1969). The unknown variables to be linearized are

$$J_1, \ldots, J_{\mathrm{NF}}, T, n_{\mathrm{e}}, n_i^{\mathrm{Hyd}}, n_{\mathrm{p}}, n_i^{\mathrm{He\,I}}, n_i^{\mathrm{He\,II}}, n_{\mathrm{He\,III}}$$

where n_x is the number density of electrons, protons, NLTE-levels of hydrogen, He I, He II and He III. To improve convergence each complete linearization is followed by an internal ALI-cycle for J_k and occupation numbers holding the temperature fixed.

Because of Eq. (6) our system is depth coupled and therefore limited to roughly of 100 frequency and 90 depth points if our model is to be calculated with a reasonable amount of computer time.

ii) Accelerated Lambda iteration (ALI)

We use Eq. (11) where the ALI calculation of mean intensity by Eq. (4) is explicitly taken into account. Thus the depth coupling through the transfer equation is dropped and a much smaller remaining system has to be linearized allowing many more frequency and/or depth points to be considered. This aspect will be important for future work with respect to the inclusion of metals.

In every case we need a "formal solution" for the complete linearization to obtain the quantities f_k^d and q_k^d that are then held fixed, as well as to provide starting values of J_k^d at every depth and for every frequency for the ALI procedure.

The formal solution is performed in $p-z$ geometry (see for instance Puls, 1987). Here we solve:

$$\frac{u^{d-1}}{\Delta\tau^{d-\frac{1}{2}}\Delta\tau^d} - \frac{u^d}{\Delta\tau^d}\left(\frac{1}{\Delta\tau^{d+\frac{1}{2}}} + \frac{1}{\Delta\tau^{d-\frac{1}{2}}}\right) + \frac{u^{d+1}}{\Delta\tau^{d+\frac{1}{2}}\Delta\tau^d} = u^d - S^d. \quad (12)$$

Equation (12) is a monochromatic transfer equation (we suppress the frequency index k) for given source function S^d and the symmetric Feautrier variable u^d:

$$u^d = u^d(z, p) = \frac{1}{2}(I^+(z, p) + I^-(z, p)) \quad (12a)$$

with I^+, I^- being specific intensities in the positive and negative z direction,

$$\Delta\tau^{d-\frac{1}{2}} \equiv \Delta\tau^{d-\frac{1}{2}}(z,p) = \tfrac{1}{2}(\chi^d + \chi^{d-1})(z^d(p) - z^{d-1}(p))$$

$$\Delta\tau^{d+\frac{1}{2}} \equiv \Delta\tau^{d+\frac{1}{2}}(z,p) = \tfrac{1}{2}(\chi^{d+1} + \chi^d)(z^{d+1}(p) - z^d(p)) \tag{12b}$$

and

$$z(p) = (r^2 - p^2)^{\frac{1}{2}}.$$

Solving Eq. (12) with the help of a Rybicki-like algorithm (see Mihalas and Hummer, 1974) we can easily obtain the desired quantities J^d, f^d or q^d by

$$K^d = \frac{1}{r_d^3}\int_0^{r^d} u(z,p) z^2\,\mathrm{d}z$$

$$J^d = \frac{1}{r_d}\int_0^{r^d} u(z,p)\,\mathrm{d}z \tag{12c}$$

and by application of Eqs. (8), (9).

Both procedures work satisfactorily and converge to the same results. However, in a few cases one or other of the two seems to be more stable. Particularly for objects close to the Eddington limit it is difficult to say a priori whether the complete-linearization code or the ALI-code is superior. Consequently, both procedures have been used. (We will, however, systematically investigate the behaviour of the ALI-code for the future work.)

2.4. *Subsequent line radiation transfer in the comoving frame*

To test the Sobolev approximation we have performed additional line radiation transfer calculations in the comoving frame. Particularly in the low velocity region, where $v(r) < v_{\text{sound}}$, the condition that the region where the radiation and matter interact should be small enough to guarantee no noticeable change in the level populations, and therefore in integrated line opacity and the line source function, is no longer fulfilled. The correct way of treating the line radiation transfer problem is to transform into the comoving frame (CMF), to solve the equations there and then to perform a backtransformation of the quantities of interest to the observer's frame (see Mihalas et al., 1975).

The equation of radiative transfer in the CMF is written in the following form, where terms in order of $(v/c)^2$ have been dropped:

$$\mu\frac{\partial}{\partial r}I(\nu,\mu,r) + \frac{1-\mu^2}{r}\frac{\partial}{\partial\mu}I(\nu,\mu,r) - \frac{v_0 v(r)}{c\,r}\left(1-\mu^2+\mu^2\frac{\mathrm{d}\ln v(r)}{\mathrm{d}\ln r}\right)$$
$$\times\frac{\partial}{\partial\nu}I(\nu,\mu,r) = \eta(\nu,r) - \chi(\nu,r)I(\nu,\mu,r). \tag{13}$$

η and χ are the total emissivity and opacity, line plus continuum.

This equation is numerically solved in the usual $p-z$ geometry (see above) to yield the profile weighted mean intensity

$$\bar{J} = \int_0^1 \mathrm{d}\mu \int_{-x_{\max}}^{x_{\max}} \mathrm{d}x\,\phi(x,r)u(x,p,z) \tag{14}$$

x is the frequency displacement from the line centre in the comoving frame in units of the Doppler width (for details see Hamann, 1986 or Puls, 1987).

The line profile in the CMF is symmetric; $x_{\max}$ is chosen as a few units of the thermal Doppler width to guarantee that the ratio of the line opacity to the continuum opacity is less than e.g. 10^{-3} at $x = \pm x_{\max}$. The profile function $\phi(x,r)$ is given by the thermal Doppler profile, normalized so that

$$\int_{-x_{\max}}^{x_{\max}} \mathrm{d}x\,\phi(x,r) = 1.$$

Equation (14) yields $\bar{J}(r)$ in the comoving frame. Now one should perform a backtransformation to the observer's frame, but the error is only of the order of v/c and amounts to a maximum of about 1% of $\bar{J}(r)$ at $r = R_{\max}$.

The line radiation rates are normally given in the following form

$$R_{ij} = B_{ij}\bar{J}$$

$$R_{ji} = A_{ji} + B_{ji}\bar{J}$$

Thus a comoving frame ALI-method is used (see Hamann, 1985). The local operator Λ^* is chosen in the following way:

We define two frequencies x_{red} and x_{blue} (depth dependent) that separate the optically thick line core from the wings. Then the "core fraction" f_{C} denotes the part of the scattering integral, that belongs to the line core:

$$f_{\text{C}} = \int_{x_{\text{red}}}^{x_{\text{blue}}} \phi(x)\,\mathrm{d}x \Big/ \int_{-x_{\max}}^{x_{\max}} \phi(x)\,\mathrm{d}x. \tag{16}$$

The operator Λ^* is set equal to f_{C} and becomes a simple multiplication in this case:

$$\Lambda^* S = f_{\text{C}} S.$$

For more detailed information see e.g. W. R. Hamann, 1985. The ALI-method is used in the form described above

$$\bar{J}^{\text{new}} = \bar{J}^{\text{FS}} + f_{\text{C}}(S_{\text{L}}^{\text{new}} - S_{\text{L}}^{\text{old}})$$

The line radiation rates can then be written in the following form:

$$R_{ij} = B_{ij}\bar{J}^{\text{FS}}$$

$$R_{ji} = A_{ji} + B_{ji}\bar{J}^{\text{FS}} + f_{\text{C}}A_{ji}\left(\frac{S_{\text{L}}^{\text{old}} - S_{\text{L}}^{\text{new}}}{S_{\text{L}}^{\text{old}}}\right). \tag{17}$$

S_{L} is the line source function under the assumption of complete redistribution.

The upward rate keeps its original form whereas in the downward rate an additional term appears. $\bar{J}^{\text{FS}}$ is the solution of the above equation of line transfer in the CMF with known opacity χ.

The iteration cycle works as follows:

— Formal solution of continuum radiation transfer with the Rybicki algorithm to yield $\bar{J}^{\text{FS}}$, the radiation field in the continuum, and u_{c}, v_{c} for the blue wing boundary condition in the CMF

— Formal solution of line radiation transfer in the CMF to get $\bar{J}(r)$

— calculation of the line and continuum radiative transition rates at each depth point with the "new" ALI-method, followed by a solution of the statistical equations. This yields new occupation numbers and the iteration cycle is started again.

As soon as the relative corrections of the level populations and the radiation field have reached a certain convergence limit, the "emergent" line profile is calculated by a formal integral of the equation of radiative transfer.

The line profile is given by the ratio of total flux at $r = R_{\max}$ in the direction of the observer $F^+(\bar{x}, R_{\max})$ to the continuum flux

F_c^+, the latter assumed to be constant over the line.

$$F^+(\bar{x}, R_{max}) = \frac{1}{R_{max}^2} \int_0^{R_{max}} I^+(\bar{x}, R_{max}, p)\, p\, dp, \tag{18}$$

where $\bar{x}$ is the Doppler normalized frequency in the observer's frame between

$$\bar{x}_{min} = \min(-X_{max} + \mu V) = -X_{max} - \mu^* V_{max}$$

$$\mu^* = \left(1 - \left(\frac{R_*}{R_{max}}\right)^2\right)^{1/2} \tag{19a}$$

and

$$\bar{x}_{max} = \max(X_{max} + \mu v) = X_{max} + V_{max}. \tag{19b}$$

The velocity v is measured in units of v_{th} and $X_{max} \approx 4$.

In the backward direction, part of the stellar envelope is hidden by the stellar core and therefore only $\mu^* V_{max}$ contributes to $\bar{x}_{min}$. The quantity $I^+(\bar{x}, R_{max}, p)$ is given for each p-ray by a formal solution of the radiative transfer equation, evaluated at $r = R_{max}$.

$$I^+(\bar{x}, R_{max}, p) = \int_{z_{min}}^{z_{max}} \chi(\bar{x} - \mu\, v, z') S(\bar{x} - \mu\, v, z') \exp(-\Delta\tau(\bar{x} - \mu v, z'))\, dz' + \begin{cases} I_C \exp(-\Delta\tau(\bar{x} - \mu v, z(R_*))) & p \le R_* \\ 0 & p > R_*. \end{cases} \tag{20}$$

χ, S are the total opacity and source function, line plus continuum, and $\Delta\tau = -\int_{z_{max}}^{z} \chi(z')\, dz$ is the optical depth on a specific ray p from the first point $z_{max} = (R_{max}^2 - p^2)^{\frac{1}{2}}$ to a point z on the ray. z_{min} is given by:

$$z_{min} = \begin{cases} (R_*^2 - p^2)^{\frac{1}{2}} & p \le R_* \\ -z_{max} & p > R_*. \end{cases}$$

In the formal solution for the final emergent line profile we allow for full Stark broadening of the hydrogen and helium lines in the entire sub and supersonic atmosphere as is normally done in plane-parallel hydrostatic models. Thus the contribution of Stark broadening in the deeper layers combined with wind emission and "wind-velocity broadening" is treated correctly. This is of course only possible in our unified models, in which the artificial division between winds and hydrostatic photosphere is avoided. Test calculations have shown that the shapes of the emergent profiles change noticeably if Stark broadening is taken into account in cases where the wind emission is not totally dominant. This effect has not been considered correctly in previous work (see introduction). For the Stark broadening of the hydrogen lines the theory of Vidal et al. (1973) is used. The recent extension of this theory by Schöning and Butler (1989a, b) including the effects of ionic charges on the paths of the perturbers is applied in the case of He II.

3. Models for the O4f star ζ Puppis

The O4f star ζ Puppis is an ideal example for the application of our calculations. This well observed bright object exhibits well defined "photospheric" absorption profiles simultaneously with the typical emission lines of Of stars that are attributed to the stellar wind. The quantitative analysis of the photospheric profiles by means of detailed plane-parallel NLTE calculations allowed a precise determination of the effective temperature and gravity (Kudritzki et al., 1983; Bohannan et al., 1986). The UV wind lines, the wind free-free emission in the radio and infrared spectral range are observationally well studied (Lamers and Morton, 1976; Hamann, 1980; Morton and Wright, 1979; Lamers et al., 1984). Detailed radiation driven wind models including full NLTE and multi-line effects have been computed and roughly reproduce the observed v_∞ and $\dot{M}$ and the high ionization features of N V and C IV (Pauldrach, 1987a, b; Puls, 1987a, b). We have therefore calculated our first "unified" models for stellar parameters representative of this object in Table 1.

The first choice of parameters (model A) uses the results of Bohannan et al., based on new CCD observations of very high S/N. However, these parameters were obtained using plane-parallel hydrostatic NLTE models for the profile fit, including the effect of wind blanketing. It is important to realize that our models do still not account for this effect: They include the presence of thousands of metal lines only in the calculation of the radiative acceleration for the treatment of the radiation hydrodynamics but neglect the metal line opacity in the radiative equilibrium and in the calculation of the local mean density J_ν (see also Sect. 2). As pointed out by Abbott and Hummer (1985) and Bohannan et al. it is necessary to increase T_{eff} and $\log g$ for models without wind blanketing to produce similar photospheric lines and UV emergent flux. This is the reason for the second set of stellar parameters in our calculations (model B). The line force parameters are $k = 0.053$, $\alpha = 0.709$, $\delta = 0.052$, obtained by Pauldrach (1987a, b, see also Puls, 1987a, b). The hydrodynamic radiation driven wind calculations then yield for every model the values of $\dot{M}$ and v_∞, also given in Table 1. A normal helium abundance $N_{He}/N_H = 0.1$ is adopted for both models.

The major objective of our calculations is to investigate whether the strategic photospheric lines for the NLTE determination of stellar parameters (Hγ, Hδ,He II λλ 4542, 4200) are contaminated by wind emission. Moreover, it is important to find out if the calculations can at least qualitatively reproduce the observed emission of Hα and He II 4686 and the excess of far infrared radiation.

3.1. *Atmospheric structure*

First we compare the structure of the spherical extended unified models with conventional plane-parallel hydrostatic models. The natural depth variable, on which the latter are physically defined, is the Rosseland optical depth τ_{Ross}. Consequently we have chosen τ_{Ross} as depth variable for this comparison. Figure 1 gives an impression of the spherical extension of the atmosphere and of the region where the velocity field becomes important. It is evident that in the region where the continuum between 228 Å and 10 000 Å is formed, sphericity and the velocity field are unimportant. On the other hand, continuum photons with

Table 1. Stellar parameters and self-consistently computed $\dot{M}$ and v_∞ for the ζ Pup models

Model	T_{eff}	$\log g$	$R/R_\odot$	$\dot{M}(M_\odot\,yr^{-1})$	$v_\infty(km\,s^{-1})$
A	42 000 K	3.5	19	$4.40\,10^{-6}$	2042
B	45 000 K	3.6	18	$5.94\,10^{-6}$	2196

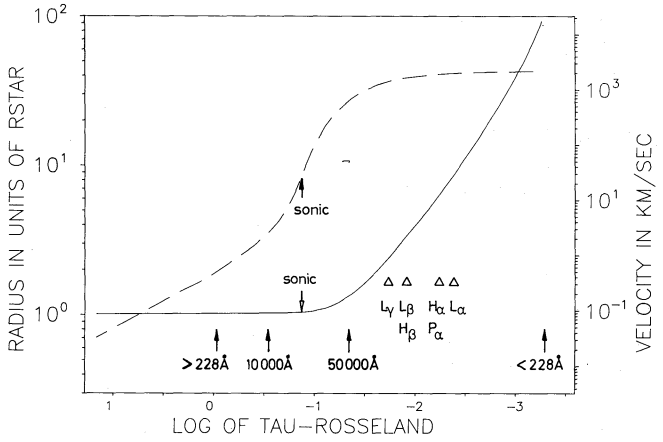

Fig. 1. Stellar radius r/R_* (fully drawn) and wind outflow velocity v (dashed) as a function of log τ_{Ross} for model B. The arrows indicate the sonic point and the depths where $\tau_\nu = 1$ is reached for the corresponding wavelength. Triangles mark the depth where the cores of important lines become optically thin in the corresponding hydrostatic model

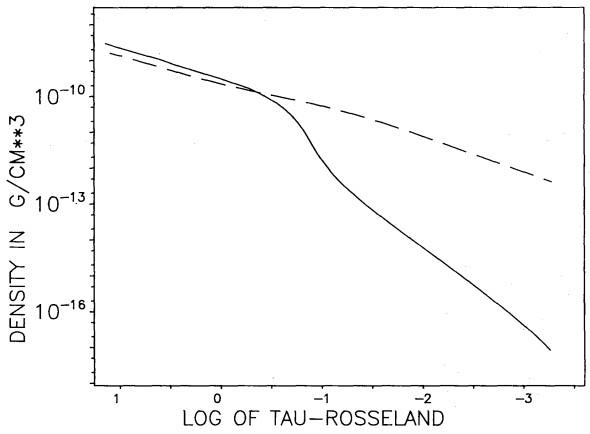

Fig. 2. Mass density ρ versus log τ_{Ross} for model B (fully drawn) and the corresponding plane-parallel hydrostatic model (dashed)

$\lambda < 228$ Å and $\lambda > 50\,000$ Å are clearly formed in regions affected by spherical extension and the velocity field. In addition, we expect Hα, He II 4686, Hβ and the infrared hydrogen and helium lines to be contaminated by wind emission.

Figure 2 shows the density stratifications. The difference in density in the supersonic part of the unified model is evident. The small difference between hydrostatic and unified models in deeper layers ($\tau_{\text{Ross}} > 1$) is a defect of the latter, since the bound-free and free-free radiative force of hydrogen and helium are neglected in the effective gravity of the stellar wind code (see PPK) and a grey temperature stratification was adopted in the deeper layers for the calculation of the density structure (see above). This will be improved in future work.

Figure 3 displays the temperature stratifications. The dilution of the radiation field due to spherical extension in the unified model is the reason for the drop in temperature below that of the plane-parallel model between $0.0 > \log \tau_{\text{Ross}} > -1.0$ (see also Mihalas and Hummer, 1974; Gruschinske and Kudritzki, 1979). In the outer layers ($\log \tau_R \leq -2.5$) the hydrostatic model shows

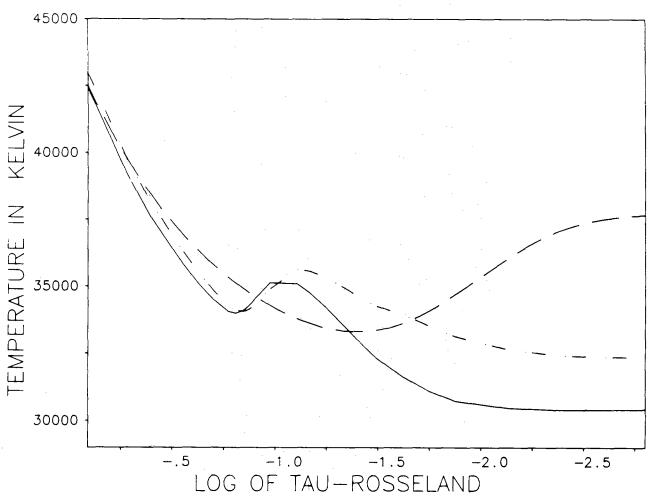

Fig. 3. Temperature versus log τ_{Ross} for model B. The dashed curve represents a hydrostatic plane-parallel NLTE model (with only 6 hydrogen lines connecting the lower four levels and no helium lines). The dash-dotted curve corresponds to a unified model with 10 hydrogen lines connecting the lower 5 levels and no helium lines, whereas the fully drawn curve includes an additional 45 He II lines

the typical temperature increase due to the overpopulation of the hydrogen ground state, which is caused by the onset of line cascading as soon as the hydrogen lines become optically thin. For layers with $\log \tau_R < -3.5$ (not plotted in Fig. 3) the temperature drops again, which is due to cooling by the He II ground state continuum, which becomes optically thin there in the hydrostatic model (see Auer and Mihalas, 1972 or Kudritzki, 1979). This temperature bump is also found in the unified models, however, at much larger Rosseland optical depth $\log \tau_R \approx -1.2$. The reason for this is that due to the presence of the velocity field the lines start to desaturate close to the sonic point so that line cascading becomes important already in these layers ($\log \tau_R \approx -0.8$). This explains the increase of temperature until $\log \tau_R \approx -1.2$. The temperature drop towards lower optical depth is then again caused by cooling of the He II continuum which due to effects of the velocity field (see discussion below) also becomes optically thin in much deeper layers.

In Fig. 4 the NLTE occupation numbers are shown. We realize that both H and He are almost totally ionized throughout the important layers contributing to the optical depth (Fig. 4a). The departure coefficients of the hydrogen levels of the plane-parallel hydrostatic and unified models are very similar until the spherical extension becomes important. Then the geometrical dilution of the ionizing radiation in the Lyman continuum causes the ground state departure coefficients to increase, whereas the populations of the excited levels are dominated by the downward electron cascades and thus remain roughly unaffected by the dilution (Fig. 4b).

An important effect is seen in the He II ground state departure coefficient (Fig. 4c). In the hydrostatic model it increases strongly in the outer layers as soon as the continuum becomes optically thin. Hydrostatic line formation calculations including all the line transitions show the same behaviour, the result of the enormous optical thickness of all lines connected to the ground state. However, in the unified models (including the He II line transitions) we find a sharp drop in the He II ground state population

between $0.3 \geq \tau_R \geq 0.01$. This is caused by the outflow velocity field which becomes larger than the He II thermal velocity for $\tau_R < 0.3$. As a result the He II resonance line is somewhat desaturated and the high continuum radiation temperature at the frequency of this transition causes a net pumping into the first excited level, from which additional ionization occurs. As soon as the He II continuum becomes optically thin and/or the radiation field in the resonance line transition starts to become diluted, the depopulation is terminated and the He II ground state departure coefficient increases similarly to b_1 (H). This effect is, of course highly important for the continuum formation shortward of 228 Å as will be shown below. (A more detailed discussion is given in the appendix.)

Figure 4d compares the departure coefficients of the unified model with the subsequent line formation calculations in the comoving frame. As long as the number of line transitions is the same, no important effects capable of causing a significant backreaction on the temperature structure are encountered. If higher NLTE levels and correspondingly more transitions are added, the ground-state population of hydrogen increases in the outer layers, which would also lead to a mild increase of the local temperature (see also Drew, 1988).

Figure 4e shows the difference between the unified model and CMF-calculations for He II (10 levels only).

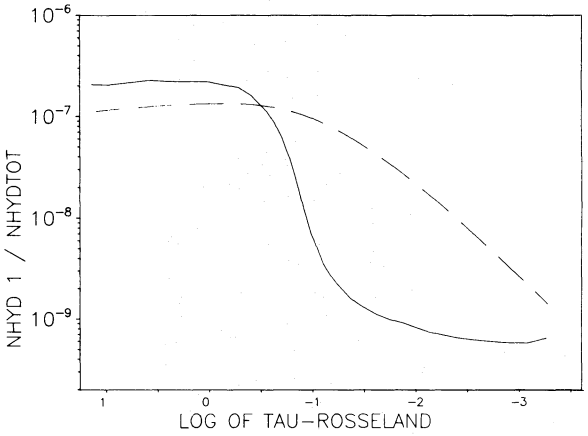

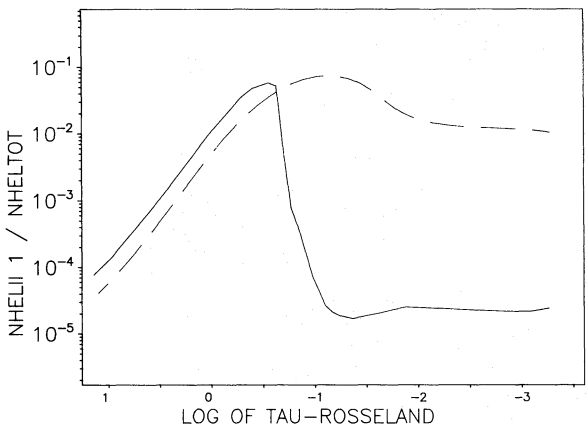

Fig. 4a. $\log n_H^1/n_H$ and $\log n_{\mathrm{He\,II}}^1/n_{\mathrm{He}}$ as a function of $\log \tau_{\mathrm{Ross}}$ for model B. Dashed: hydrostatic plane-parallel model, fully drawn: unified model

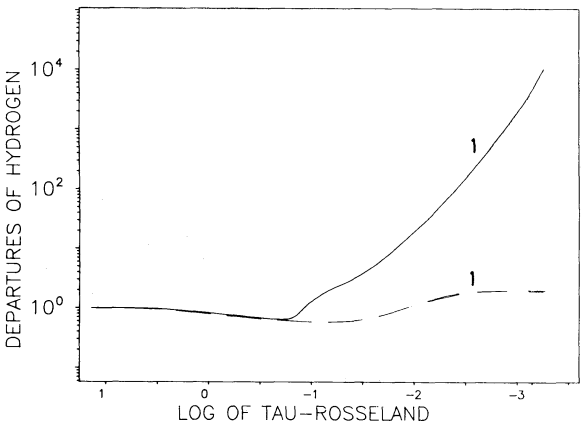

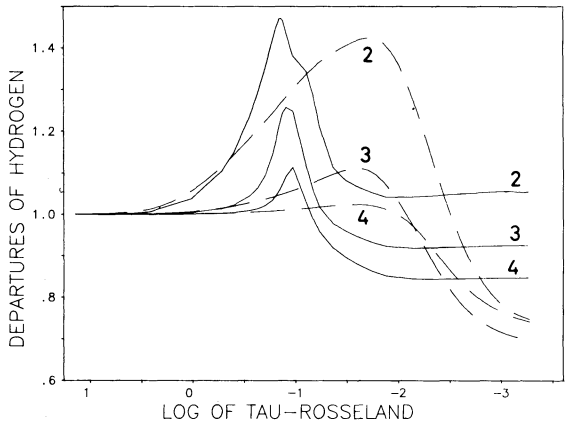

Fig. 4b. Departure coefficients of the 4 lowest levels of hydrogen as a function of $\log \tau_{\mathrm{Ross}}$. Dashed: hydrostatic plane-parallel model, fully drawn: unified model

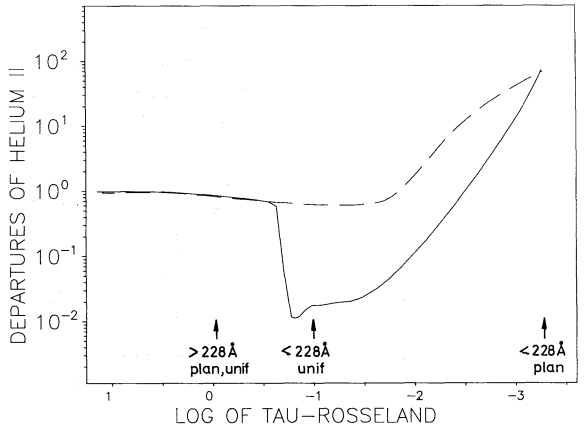

Fig. 4c. Departure coefficient of the He II ground state (logarithmic scale) as a function of $\log \tau_{\mathrm{Ross}}$. Dashed: hydrostatic plane-parallel model, fully drawn: unified model. The arrows indicate $\tau_\nu = 1$ at the frequency of the continuum edge

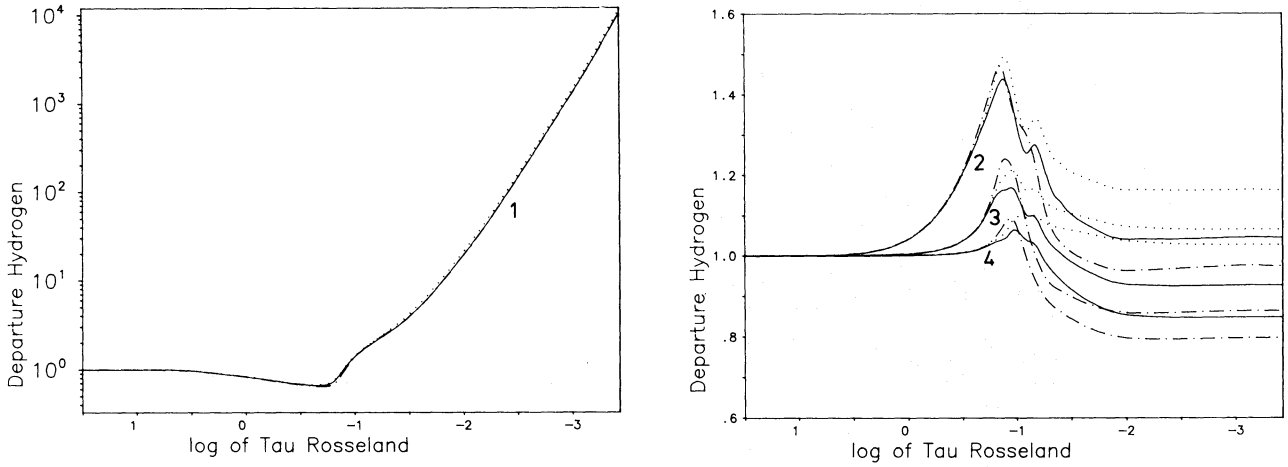

Fig. 4d. Departure coefficients of the four lowest levels of hydrogen of the unified model (dash-dotted) compared with subsequent line formation calculations in the comoving frame using the same number of NLTE level and line transitions (fully drawn) and, alternatively, 10 NLTE levels and all corresponding transitions (dotted)

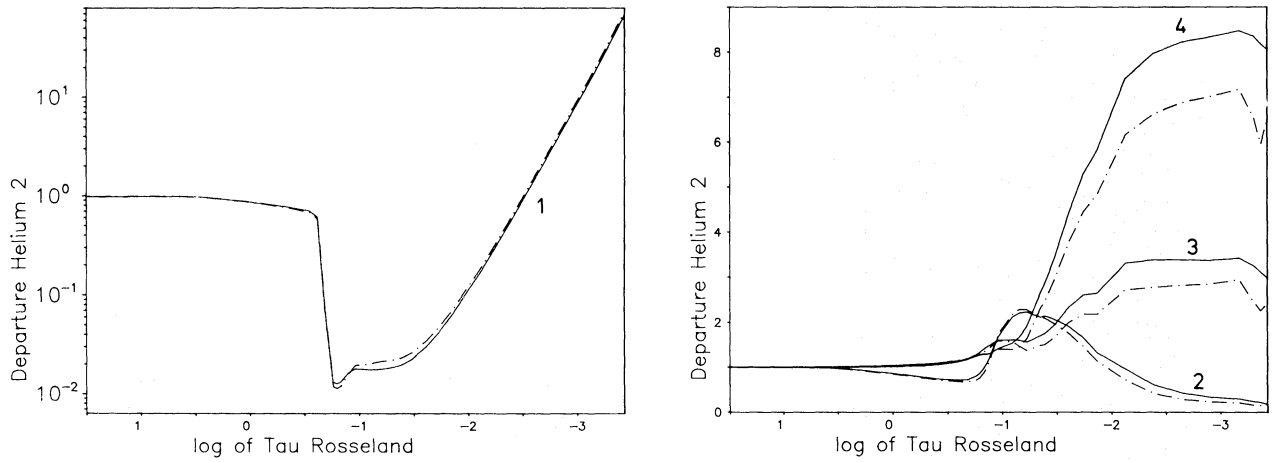

Fig. 4e. Departure coefficients of the four lowest levels of He II of the unified models (dash-dotted) compared with the comoving frame calculations using the same number of NLTE levels (fully drawn)

3.2. Energy distribution

Figure 5 compares the infrared flux predicted by the different models. While the hydrostatic plane-parallel models show the Rayleigh-Jeans tail of the energy distribution and fail to reproduce the observations, the unified models exhibit the expected IR-excess and come much closer to the observations. The reason for the IR-excess is the enhanced free-free emission of the extended wind envelope, as has been discussed by Panagia and Felli (1975), Wright and Barlow (1975), Castor and Simon (1983), and Lamers and Waters (1984). However, while in these former treatments the density at the sonic point and the density slope entered as crucial free parameters, to be determined somehow from the observations, our unified models yield the IR-excess self-consistently without any further assumptions.

The EUV to optical energy distributions are plotted in Fig. 6. As to be expected from Figs. 1 to 4 no observable effects are present between 911 Å and 10000 Å. This explains also why hydrostatic plane-parallel NLTE models are able to fit the observed energy distribution in this spectral interval (see Kudritzki et al., 1983, Abbott and Hummer, 1985). The region between 911 Å and 228 Å is slightly affected. However, shortward of 228 Å the emergent flux in the unified model is greatly increased. This is a simple consequence of the depopulation of the He II ground state as described in the foregoing paragraph. For the ionization of the surrounding gas, as for instance in H II regions or planetary nebulae (see below), this effect will be important.

3.3. Observable H and He II lines

The emergent line profiles of some strategic lines for the detailed NLTE photospheric analysis are shown in Fig. 7. The He II Pickering lines $\lambda\lambda$ 5412, 4542, 4200 (transitions $n = 4$ to $n = 7$, 9, 11, respectively) show a decreasing degree of contamination by wind emission. λ 5412 is clearly wind affected, although it would be hard to detect this effect on the basis of observational data (see

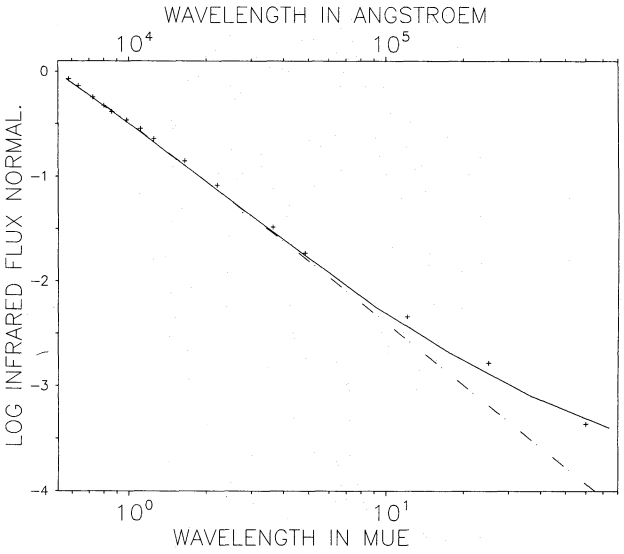

Fig. 5. IR energy distribution for ζ Puppis of the unified models (fully drawn) and the plane-parallel models (dash-dotted). The crosses represent the observations as given by Lamers et al. (1984)

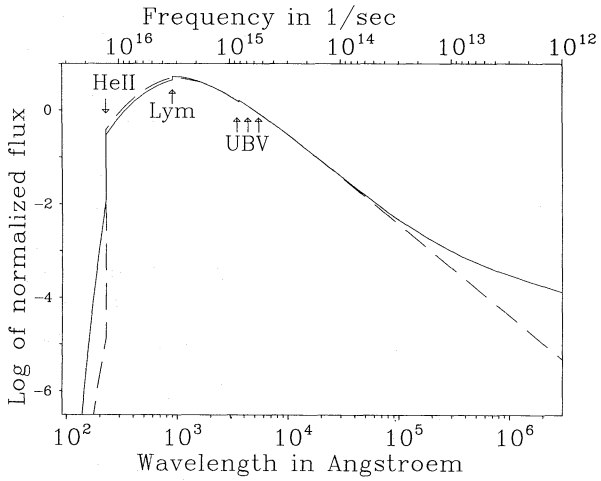

Fig. 6. EUV to visual energy distribution of the unified (fully drawn) and plane-parallel models (dashed). The He II-edge, the Lyman edge and the Johnson U, B, V bands are indicated

Bohannan et al., 1986, for the observed profile) and hydrostatic calculations only. λ 4542 exhibits wind effects only in the very core, whereas λ 4200 is almost entirely photospheric (the difference in the wing is caused by a different treatment of higher levels in the hydrostatic case). We therefore conclude that no significant errors are introduced by the use of plane-parallel hydrostatic calculations for He II 4542 and 4200.

For the important hydrogen line Hγ, normally used for the gravity determination, this conclusion (as previously made by Kudritzki et al., 1983) would be incorrect. This line is filled by weak wind emission over the entire profile. Thus, this line simply appears a little weaker due to wind effects.

For the gravity determination using hydrostatic models this means that hydrostatic gravities are systematically a little too low for objects with strong winds, e.g. Of stars. In a forthcoming paper we will study this effects in more detail.

While the effects of wind contamination are extremely moderate for the "strategic NLTE analysis lines", clear effects are found for Hβ, Hα, He II 4686 and He II 1640. This is demonstrated by the profiles given in Fig. 8, where the large difference between the old hydrostatic and our new unified models is obvious. (In passing we note that He II 4686 roughly agrees with the observed profiles, whereas the Hα emission predicted by this unified model is still too weak. The case of He II 1640 is doubtful because of blends in the UV spectrum. (A detailed comparison with observations will be carried out in a subsequent paper).

Since the modern observational techniques also allow precise line profiles of infrared lines to be observed, we show profiles of He II 10 124 Å, Pα and Bα in Fig. 9. These are obviously all wind lines.

4. Models for central stars of planetary nebulae

The detailed quantitative NLTE spectroscopy of Central Stars of Planetary Nebulae (CSPN) using high resolution, high signal to noise spectra has recently allowed effective temperatures, gravities, helium abundances, mass and radii of a large sample of CSPN to be determined with surprising precision (Méndez et al., 1988; Méndez, 1988; Kudritzki and Méndez, 1988). Three questions arise from this work: First, do the effects of spherical extension and stellar winds affect the lines used for the NLTE analysis? (Note that Central Stars have often the same photospheric scale height as massive O stars but much smaller radii.) Second, are the unified models able to reproduce the systematic occurrence of He II 4686 and Hα in emission for objects close to the Eddington limit? Third, how strongly is the shape of the continuous energy distribution affected? Can the unified models solve the long-standing problem of the "He II Zanstra discrepancy", a statement of the fact that plane-parallel hydrostatic models in many cases predict orders of magnitude less photons in the He II continuum than observationally inferred from He II nebular emission lines. To investigate these questions we have calculated a sequence of models for CSPN with $T_{\rm eff} = 50\,000$ K and different stellar masses between $0.55\,M_\odot$ to $1.0\,M_\odot$. The stellar parameters are given in Table 2. The stellar wind force multiplier parameters are adopted from the recent wind calculations for CSPN by Pauldrach et al. (1988). For $0.55\ M_\odot \le M \le 0.85 M_\odot$, $k = 0.092$, $\alpha = 0.653$, $\delta = 0.035$ were used, whereas for $1\ M_\odot$, $k = 0.170$, $\alpha = 0.655$, $\delta = 0.046$ were chosen.

The radii follow from the core-mass luminosity relation of post Asymptotic Giant Branch stars (Schönberner, 1983, Wood and Faulkner, 1986). As indicated by Table 2 the CSPN come closer to the Eddington luminosity $L_{\rm E}$ with increasing mass. Thus, our sequence of models will allow the importance of sphericity and winds as a function of distance from the Eddington limit to be investigated.

4.1. *Atmospheric structure*

Figure 10 summarizes the results with respect to the atmospheric structure. As was to be expected, the degree of atmospheric extension increases with increasing stellar mass because of the increasing pressure scale height and the stronger and denser winds when approaching the Eddington limit (Fig. 10a). The sonic point moves inward with respect to the Rosseland optical depth so that the influence of the outflow velocity field comes

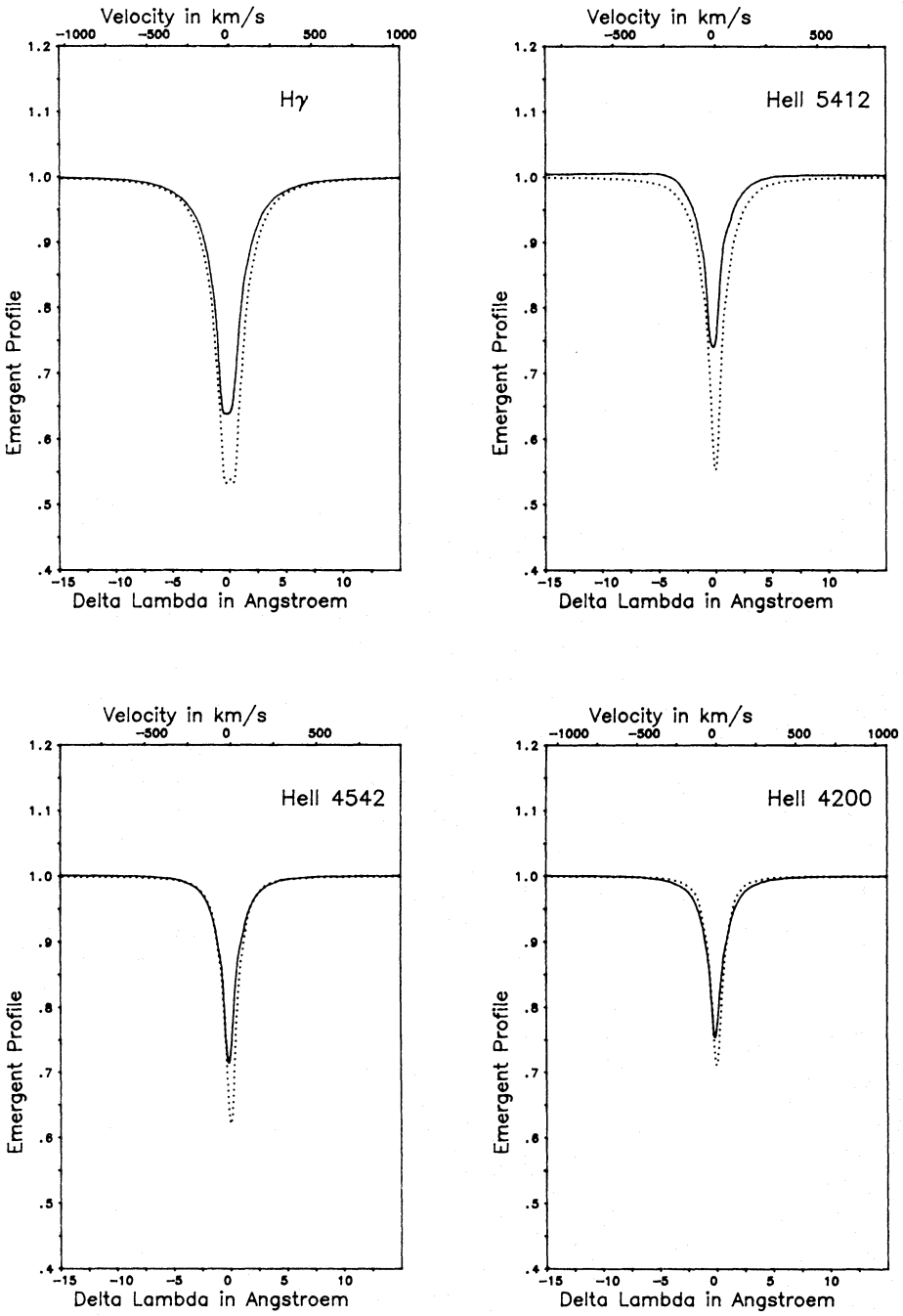

Fig. 7. Profiles of Hγ, He II 5412, 4542, 4200 of the comoving frame calculations (fully drawn) and hydrostatic plane-parallel models (dotted)

close to the region of continuum formation in the most extreme case (Fig. 10b). The temperature stratification reflects the increasing degree of atmospheric extension and geometrical dilution of the radiation field (Fig. 10c). The hydrogen departure coefficients are affected in a similar way (Fig. 10d) and the sudden decrease of the He II ground state population due to the onset of the outflow of atmospheric matter is present in all models where the He II lines have been included in the rate equations (Fig. 10e). This will have important consequences for the He II Zanstra discrepancy.

4.2. *Spectral lines*

We have calculated line profiles of Hγ and He II 4542 as typical photospheric lines and Hα and He II 4686 as lines, characteristic of those observed to switch from absorption to emission as the stellar parameters approach the Eddington limit (Kudritzki and Méndez, 1988). Figure 11 shows Hγ and He II 4542. Surprisingly, a weak difference between the hydrostatic and the unified models is already present in the wings of Hγ at 0.55 and 0.65 $M_\odot$. In our forthcoming work we will have to check whether this is caused by small systematic numerical differences of the models or really by sphericity and winds. The distortion of the profiles by the winds is obvious for the models with $M \geq 0.75\, M_\odot$. A careful investigation will be needed to disentangle the consequences for the location of CSPN in the log g, log $T_{\rm eff}$ diagram and the stellar parameters derived from this diagram.

Hα and He II 4686 also show the observed characteristic behaviour: For lower masses the lines are mainly in absorption

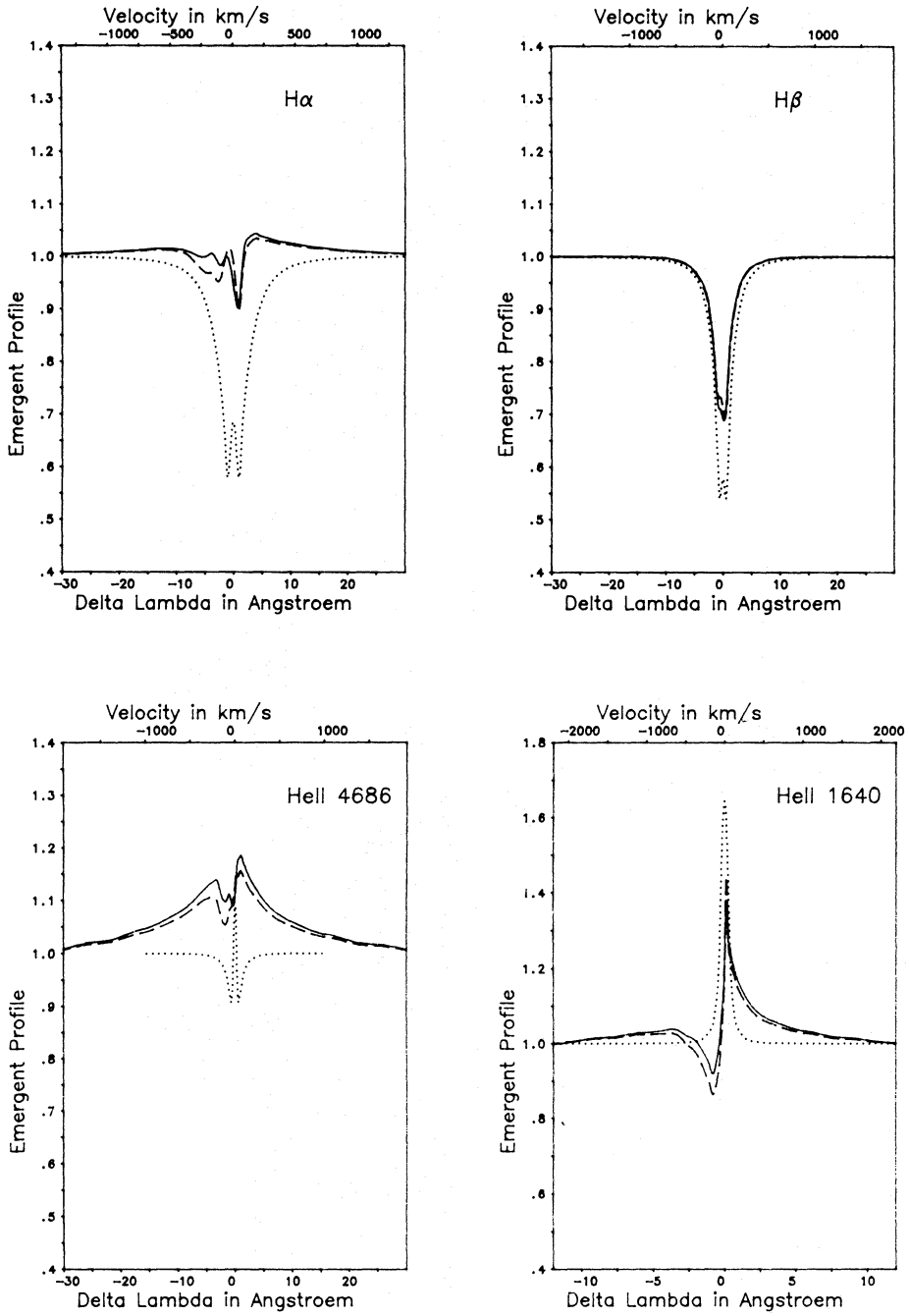

Fig. 8. Profiles of Hα, Hβ, He II 4686 and He II 1640 of the unified models (dashed) subsequent comoving frame calculations (fully drawn) and hydrostatic plane-parallel models (dotted)

(the central emission cores are normally masked by nebular emission), however at higher mass they go over into emission and become very strong at the extreme value of 1 $M_\odot$. The case of one solar mass CSPN at $T_{\rm eff} = 50\,000$ K is very close to the observed stellar parameters of NGC 2392, which according to Méndez et al., 1988 is characterized by $T_{\rm eff} = 47\,000$ K, $\log g = 3.6$, $M/M_\odot = 0.9$ and shows a very strong He II 4686 stellar emission profile.

For future spectroscopic work it will be very important to utilize the emission/absorption characteristics of He II 4686 and Hα in the spectra of CSPN as a simple tool to estimate stellar masses, radii and distances.

4.3. Energy distribution

The energy distribution of CSPN between $1200\,\text{Å} \leq \lambda \leq 10\,000\,\text{Å}$ is frequently used to determine stellar temperatures. Although this is a doubtful method for hot objects because of the Rayleigh-Jeans character of the energy distribution, it is an interesting question as to whether spherical extension can cause a flattening of the spectrum and therefore simulate a lower temperature. Our calculations do not show such an effect for all models with $M \leq 0.8\ M_\odot$. However, for $M = 1\ M_\odot$ we find an extreme effect displayed in Fig. 12. This result reflects the extreme spherical extension of this model, evident in Fig. 10. Interestingly, this effect

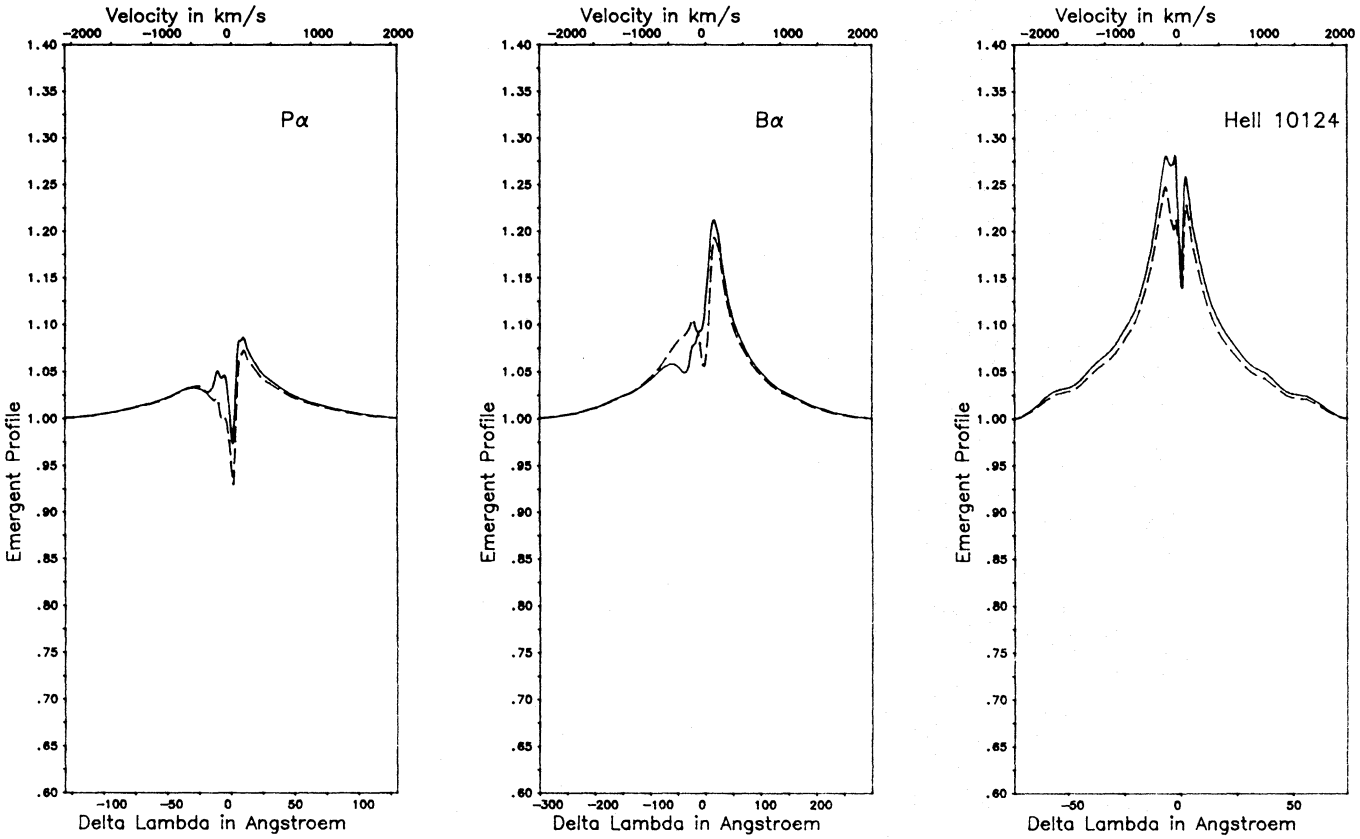

Fig. 9. Pα, Bα and He II 10 124 Å of the unified model (dashed) and the CMF calculation (fully drawn)

Table 2. Stellar parameters and computed $\dot{M}$ and v_∞ for the CSPN at $T_{\rm eff} = 50\,000$ K

$M/M_\odot$	$R_*/R_\odot$	$\log g$	$\dot{M}$ ($M_\odot$ yr^{-1})	v_∞ (km s^{-1})	$L/L_{\rm E}$
0.55	0.59	4.63	$2.86\,10^{-9}$	1658	0.09
0.64	1.24	4.06	$3.84\,10^{-8}$	866	0.35
0.75	1.62	3.89	$1.08\,10^{-7}$	635	0.52
0.85	1.90	3.81	$2.05\,10^{-7}$	520	0.62
1.0	2.24	3.74	$1.33\,10^{-6}$	426	0.74

has been observed very recently for NGC 2392 by Torres and Heap (1988).

The number of He II photons emitted with $\lambda \leq 228$ Å is another important observational quantity. Figure 13 shows that due to the effect discussed in Sect. 3 (see also Figs. 4c and 10e) the unified models with $M \leq 0.85\,M_\odot$ predict an emergent flux below the He II Lyman edge orders of magnitude larger than the one produced by the plane-parallel hydrostatic models. For the model with 1 $M_\odot$, which is very close to the Eddington limit, the wind is so dense that the depopulation of the He II ground state in the deeper layers does not affect the formation of the He II continuum. In this special case $\tau_\nu = 1$ is reached already in the outermost layers where b_1 (He II) is much larger than unity and, consequently, a strong absorption edge is obtained.

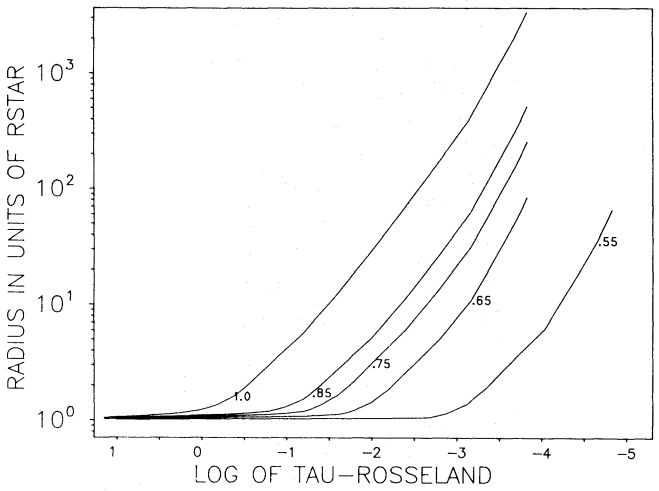

Fig. 10a. Stellar radius as a function of log $\tau_{\rm Ross}$ for different CSPN models labelled by their stellar mass

The strong increase in the emergent He II continuum flux of the unified models with $M \leq 0.85\,M_\odot$ is extremely important for the ionization characteristics of the Planetary Nebulae surrounding Central Stars. In view of the long-standing discussion concerning the He II Zanstra discrepancy (see Méndez, 1988; Kudritzki and Méndez, 1988) this is a very promising result, and motivates further detailed investigation.

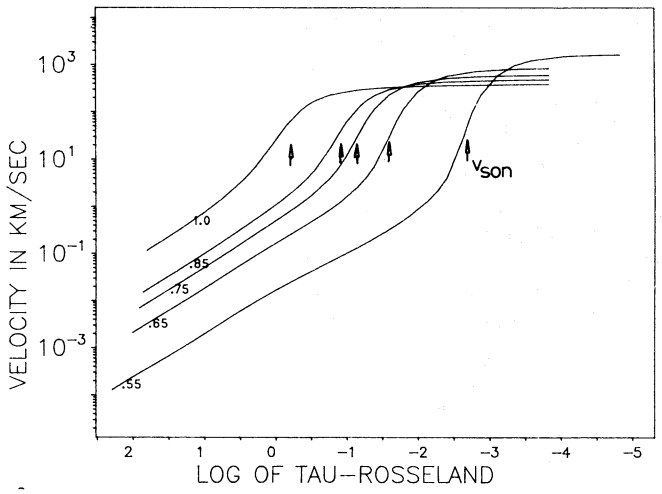

Fig. 10b. Outflow velocity versus log τ_{Ross}. The sound velocity v_s is indicated by the arrow

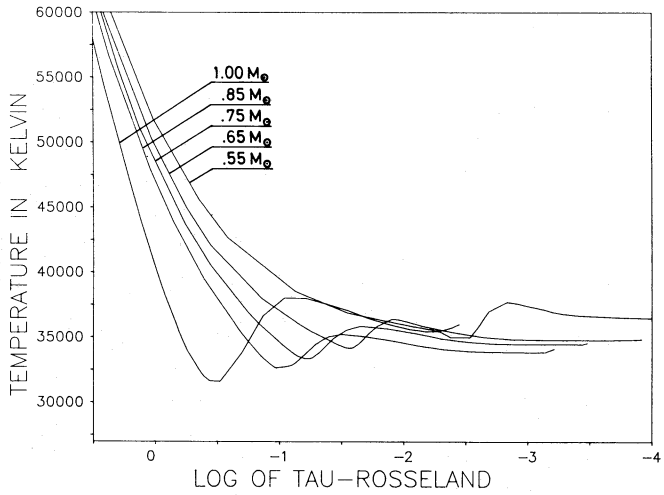

Fig. 10c. Temperature versus log τ_{Ross}

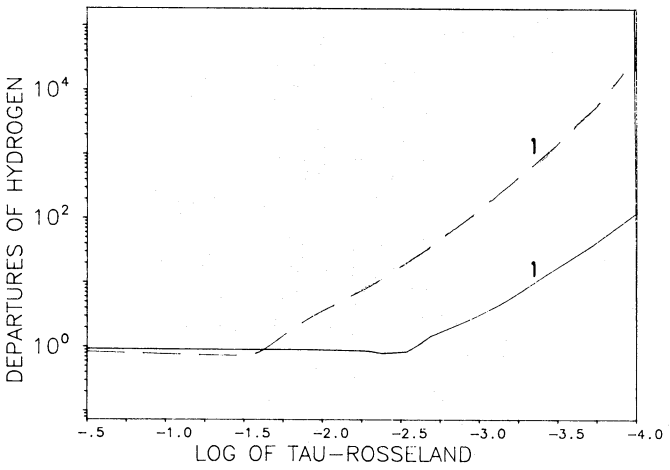

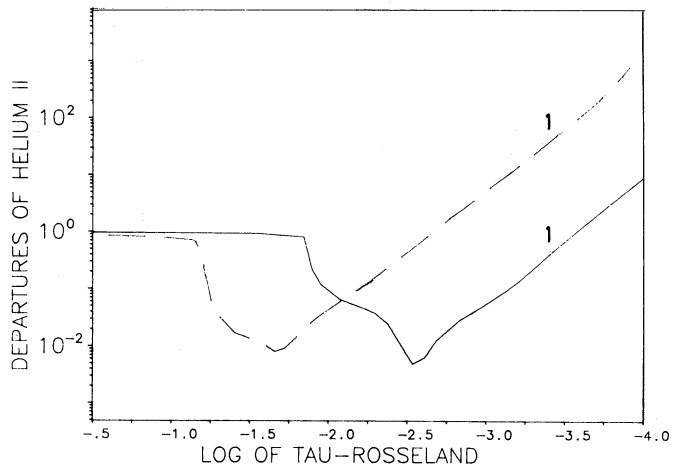

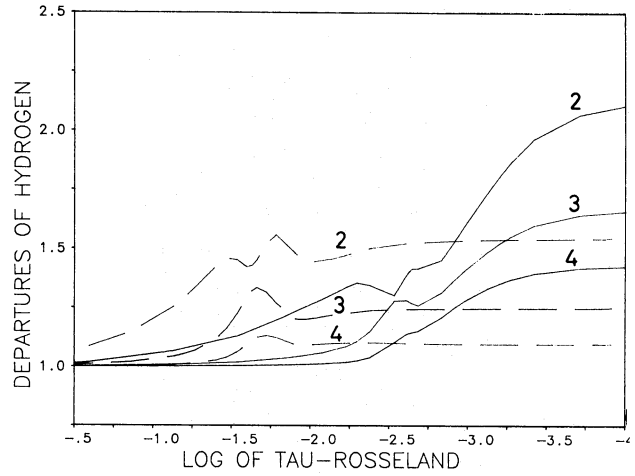

Fig. 10d. Hydrogen departure coefficients (the n value is indicated) versus log τ_{Ross} for two models ($M = 0.65\ M_\odot$, dashed, and $M = 0.55\ M_\odot$, fully drawn)

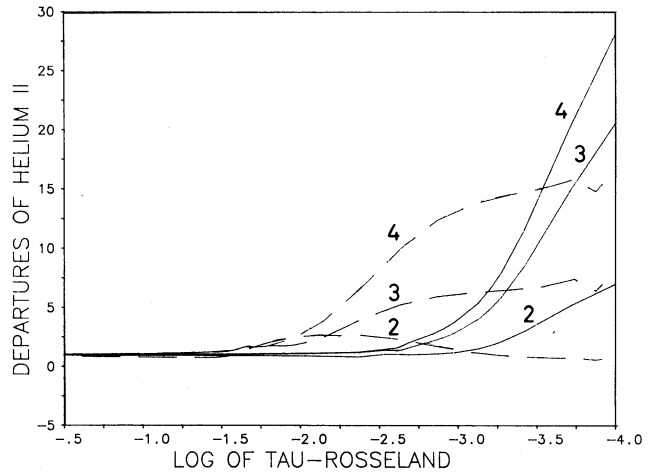

Fig. 10e. He II departure coefficient for the same models as in Fig. 10d

5. Conclusions and future work

In spite of the remaining inconsistencies of the new model the results are encouraging. While the "photospheric lines", normally used for the quantitative NLTE analysis of O stars, remain unaffected by sphericity and winds, the typical wind lines and the infrared excess are at least qualitatively reproduced by the models. An important result concerns the He II continuum. Due to the presence of supersonic wind outflow in the layers of He II continuum formation the unified models provide a factor of a thousand more photons than the conventional hydrostatic plane-parallel NLTE models. For the ionization of H II regions and Planetary Nebulae this is extremely important. The recent quantitative spectroscopy of Central Stars has clearly revealed that the He II flux predicted by the conventional models is in many cases much too low when compared with the strengths of He II 4686 nebular emission lines on the basis of recombination theory (Méndez et al., 1988, Kudritzki and Méndez, 1988). This "He II Zanstra discrepancy" is a long-standing problem (see for instance Aller, 1948; Aller and Wilson, 1954), which has cast great doubt on the validity of model atmospheres for Central Stars. Motivated by our results we will, as a first step, calculate a new grid of model atmospheres for a variety of effective temperatures and stellar masses to obtain ionizing fluxes and hydrogen and helium line profiles. We will then compare ionizing fluxes and stellar Hα and He II 4686 emission/absorption profiles with the observations of stars with well defined stellar parameters according to the analysis of the photospheric absorption lines (see Méndez et al., 1988). This comparison will reveal how reliable the new models are in a quantitative sense.

In parallel we will have to eliminate step by step the inconsistencies listed in Sect. 2: The neglect of the bound-free and free-free radiative forces in the calculation of the density structure: the iteration of the density structure after the determination of the new NLTE temperature stratification; the iteration of the force multiplier parameters k, α, δ, etc. While these are numerous but small steps, we still have one other major step to overcome: the incorporation of NLTE metal opacities in the radiative equilibrium. Since the Sobolov approximation for line transitions appears to be sufficient for this purpose, this might be proved to be easier than in the hydrostatic case (see also Pauldrach, 1987a, b). On the other hand, the bound-free radiative rates have to be computed using correct radiative transfer in spherical symmetry simultaneously with the rate equations. Here a variety of numerical difficulties will have to be overcome. With the recently developed techniques (Pauldrach and Herrero, 1988) already applied to hydrogen and helium in our new code the framework is at hand. The big questions to be answered by such self-consistent unified calculations including NLTE metal opacities are the following: How far out in the wind is radiative equilibrium valid?

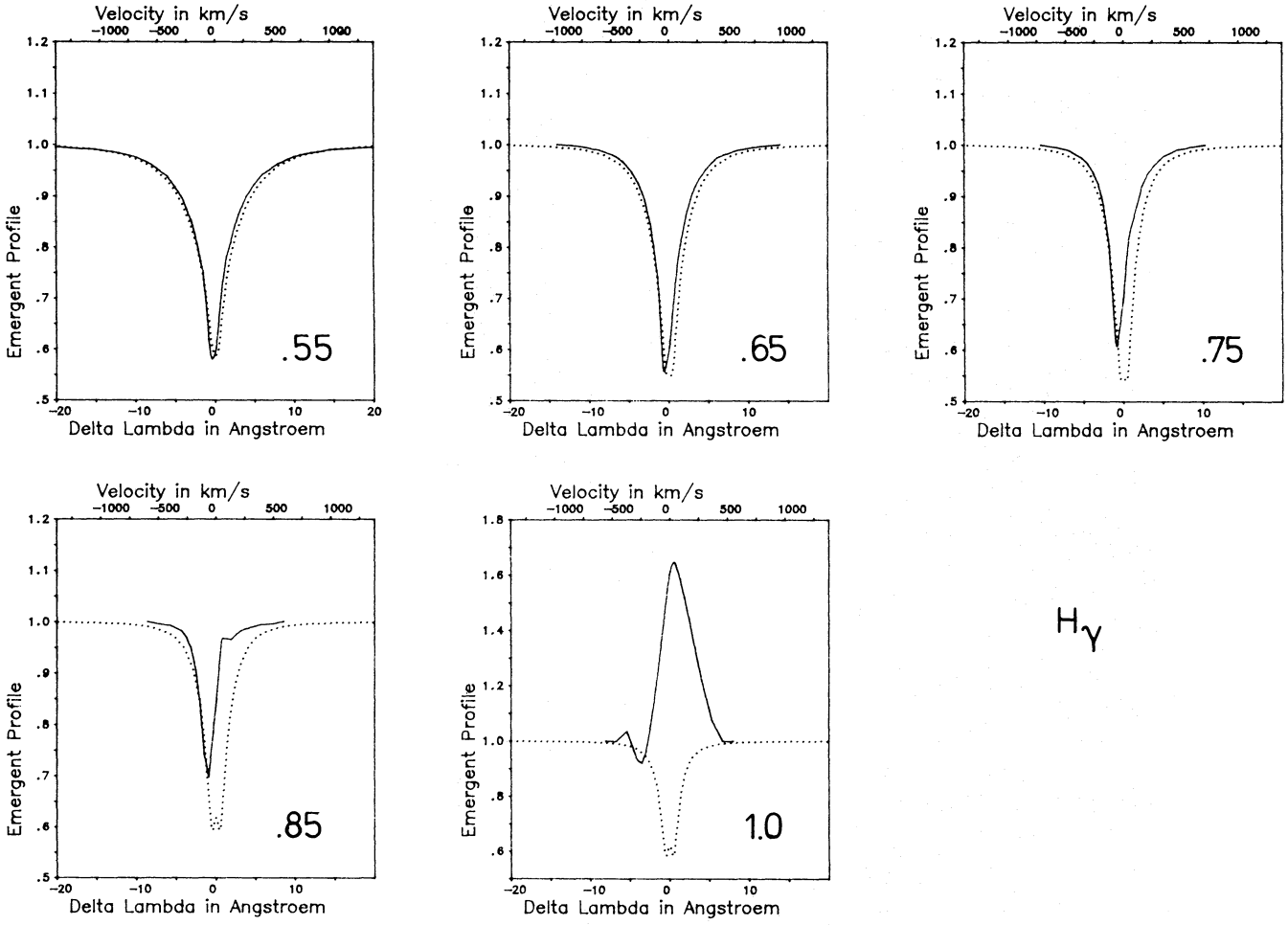

Fig. 11a. Hγ line profile for the sequence of unified CSPN models compared with hydrostatic NLTE model profiles (dotted)

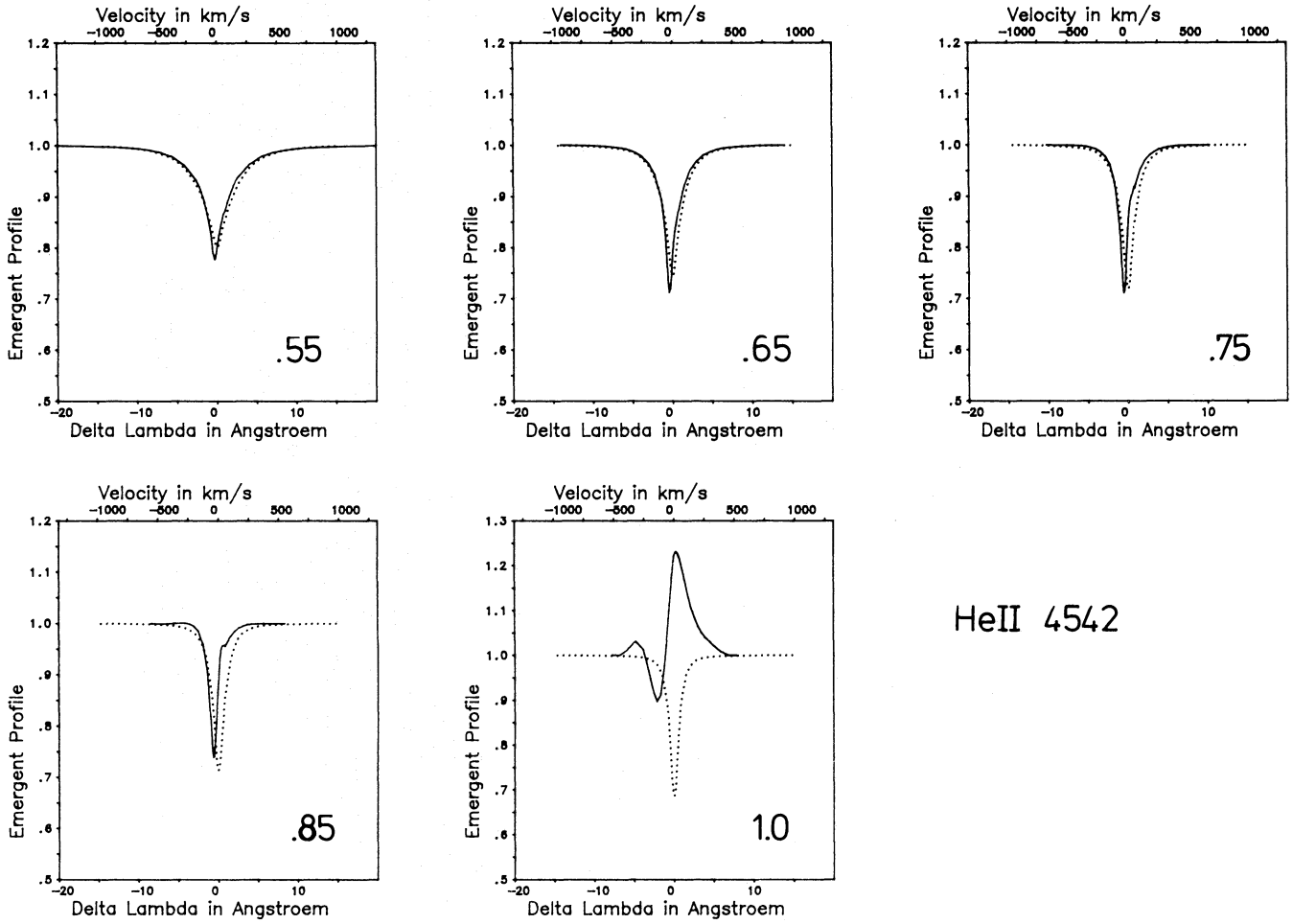

Fig. 11b. He II 4542 line profile for the sequence of CSPN unified models compared with hydrostatic NLTE model profiles (dotted)

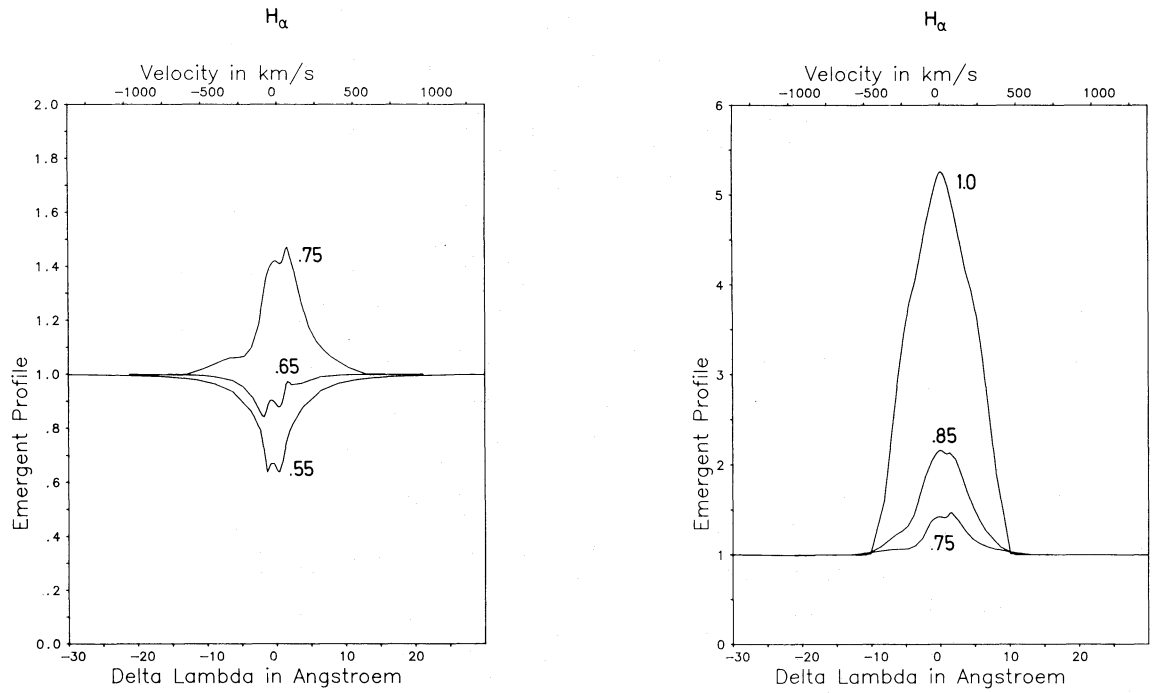

Fig. 11c. Hα line profile for the sequence of unified CSPN models

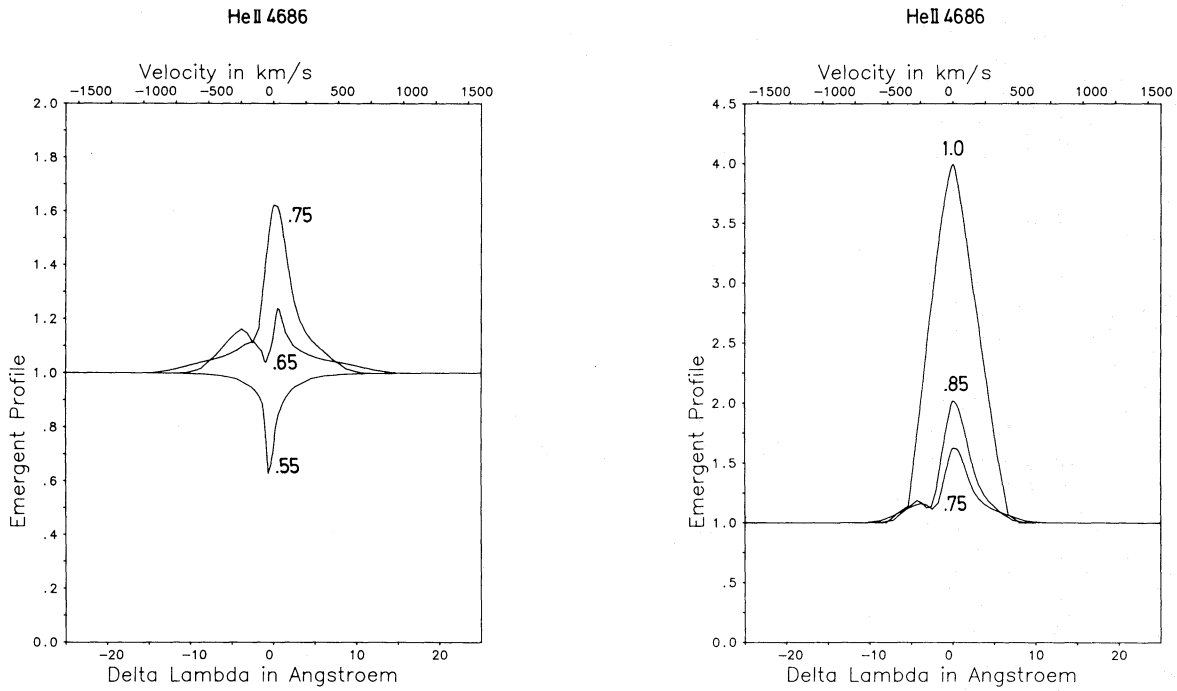

Fig. 11d. He II 4686 line profile for the sequence of unified CSPN models

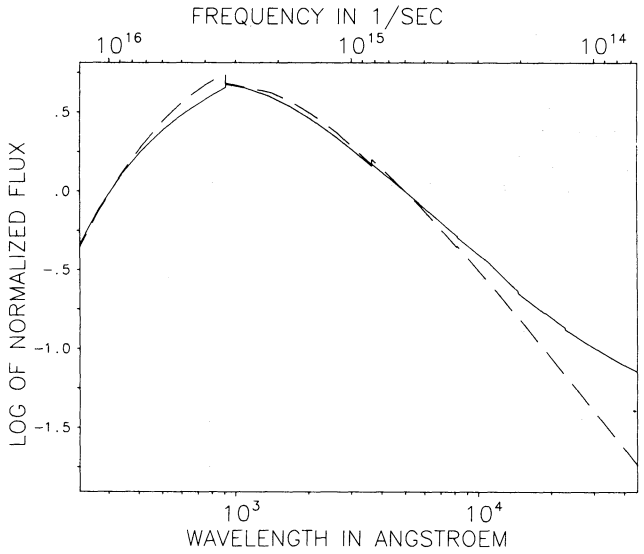

Fig. 12. EUV to IR energy distribution for the 1 $M_\odot$ unified model (fully drawn) compared with the corresponding plane-parallel hydrostatic model (dashed)

Is energy dissipation and local heating needed to keep the electron temperature in the middle and outer wind layers high enough so that the observed high ionization stages (N V, O VI) are reproduced? If yes, how much heating is needed? Note that the only way to answer these questions is in fact to calculate unified models including NLTE metal opacity and adopting the simplest approximation, proved valid in the photospheres of hot stars, namely radiative equilibrium. If it should turn out that radiative equilibrium is not valid in the outer wind layers, then by comparison with empirical temperature stratifications we would be able to estimate the amount of energy dissipated. This would be an important constraint for the description of the dissipative processes being discussed at the moment.

Having described the success and the future potential of the unified model atmospheres, let us finally also discuss their fundamental deficiences:

First and foremost, they are stationary and produce steady, monotonic flows. We are of course well aware that variability in particular in Hα but also in the P-Cygni profiles of the UV-metal lines is observed in a variety of cases. In addition, we know that the narrow absorption components observed to drift towards higher velocities over the P-Cygni profiles indicate a non-stationary, non-monotonic structure of the radiation driven winds. Moreover, the shape of the absorption part of strong P-Cygni lines has led to the conclusion that small scale velocity perturbations do exist, which can be interpreted either as "microturbulence" (Hamann, 1981a, b; Puls, 1987b; Groenewarden et al., 1989) or as "shocks" (Lucy, 1982). Our models in their present stage are not able to take these phenomena into account. We feel, however, that despite this deficiency the unified models are able to provide a reasonable description of the general time and spatial averaged behaviour of O star atmospheres, which will be useful for many astronomical applications.

On the other hand, it will be extremely important in future work to model as carefully as possible the time dependent, non-monotonic behaviour of O star winds. The very recent work by Owocki et al. (1988), though still very approximate, is an important step which indicates significant effects caused by the instabilities of line driven winds. It is evident that this approach, which at present uses a simplified description of the line force, the line radiative transfer and occupation numbers, but treats the hydrodynamic evolution and amplification of time and spatial

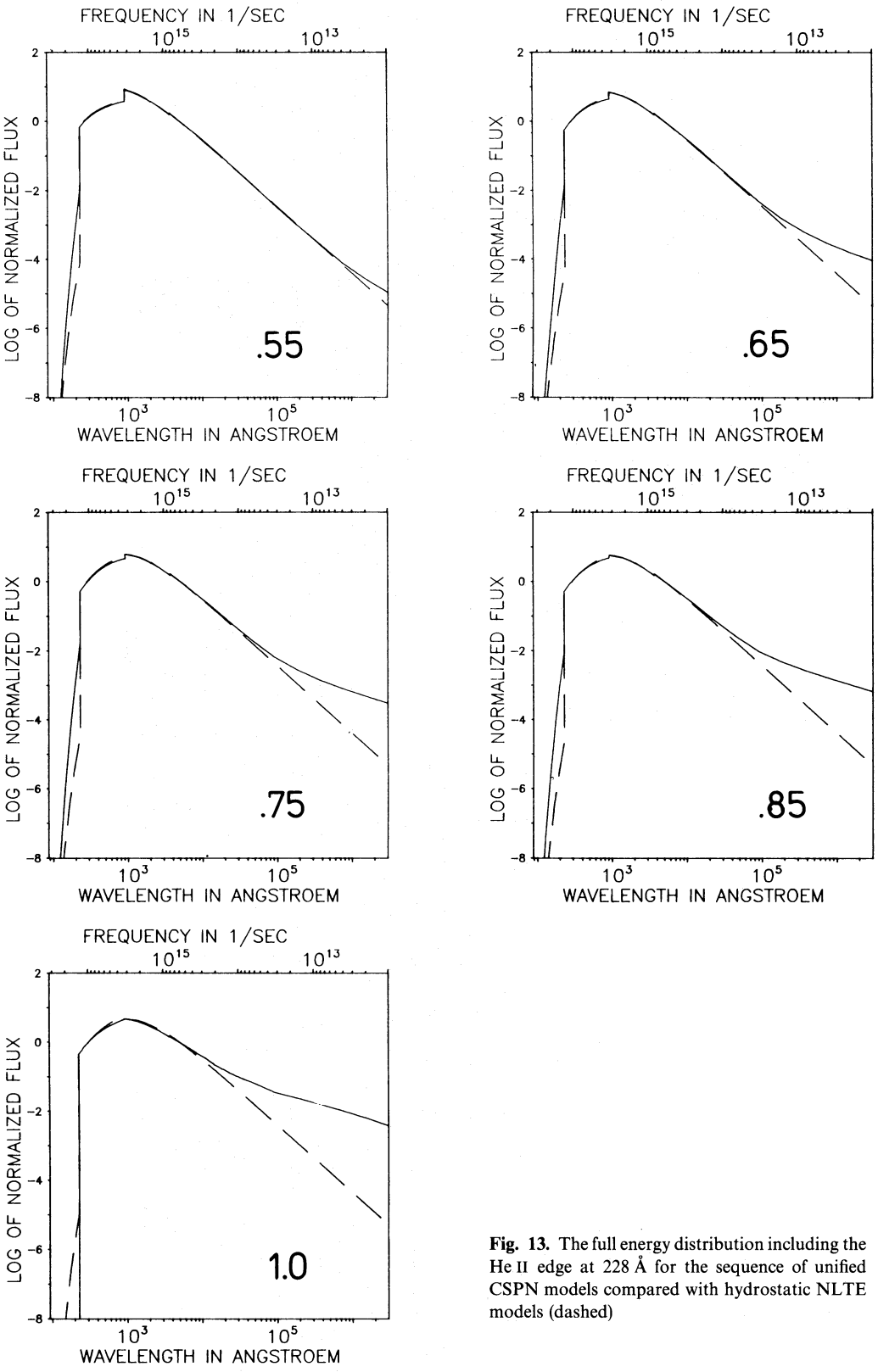

Fig. 13. The full energy distribution including the He II edge at 228 Å for the sequence of unified CSPN models compared with hydrostatic NLTE models (dashed)

dependent perturbations of the flow extremely carefully, is complementary to our procedure, which carefully calculates the NLTE radiative line force and a detailed model structure, but neglects the effects of time dependence and inhomogeneity. The differences between the two approaches should be extremely valuable in deciding the relative importance of the various physical mechanism involved. A combination of the two methods would appear to be very fruitful. Although this appears to be an

extremely complicated and laborious problem, the tools to attack it are at hand even with present day computer capacity.

Acknowledgements. It is a pleasure to thank D.G. Hummer for his continuous and encouraging support. The referees Dr. J.I. Castor and I. Hubeny helped to improve this paper by their constructive remarks. K. Butler, T. Schöning, D. Husfeld provided broadening data and useful subroutines. Their help is gratefully acknowledged. This work was supported within the DFG-Schwerpunkt "Theorie kosmischer Plasmen" under grants Ku 474-11/2 and Ku 474-13/1/2.

Appendix: the depopulation of the He II groundstate

To explain the effect of depopulation of the He II groundstate, which occurs when the He II lines are added to the rate equation, we use the Sobolev approximation for the line radiative rate, which is not too bad as the correct calculations in the CMF show. For a simplified analytical description we want to regard only the two rate equations which connect the first level with the second one:

$$b_1 R_{1k} - \left(\frac{n_2}{n_1}\right)^* b_2 A_{21} Z_{21} - R_{k1} = 0 \tag{A1}$$

$$b_2 R_{2k} + b_2 A_{21} Z_{21} - R_{k2} = 0. \tag{A2}$$

In this simplified description all collisional terms have been neglected and also all line transitions, except the resonance line between level 1 and 2. From Eqs. (A1) and (A2) we find for the departure coefficients b_1 and b_2:

$$b_1 = \frac{R_{k1} + \left(\frac{n_2}{n_1}\right)^* A_{21} Z_{21} b_2}{R_{1k}} \tag{A3}$$

$$b_2 = \frac{R_{k2}}{R_{2k} + A_{21} Z_{21}}. \tag{A4}$$

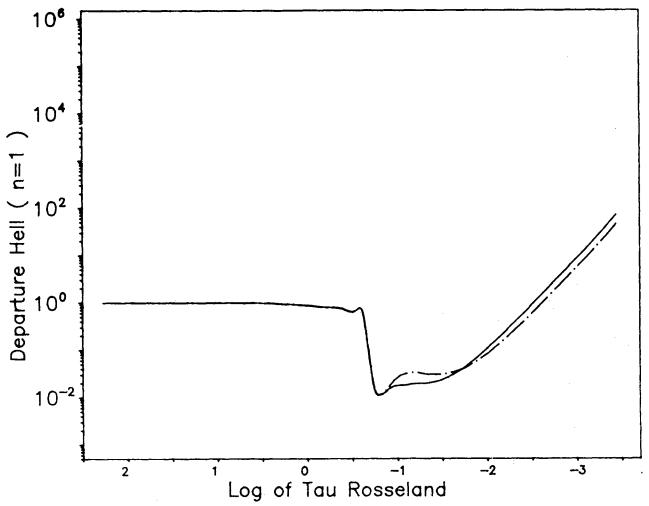

Fig. A1. Departure coefficient of the He II ground state as function of Rosseland optical depth. Solid: full numerical solution of model B (see Sect. 3). Dashed-dotted: simplified formula of Eq. (A3)

Figure A1 shows the application of equation (A3) to the final converged model. The approximate result deviates only slightly from the correct curve, which justifies the simplifications we have made. Z_{21} here denotes the line net radiative rate and is dependent on the escape probabilities β, β_c, the line source function and the incident intensity I_c of the continuum near the line frequency ν_0. Assuming an analytical velocity field ($v \approx v_\infty(1 - R_*/r)$) for the calculation of β and β_c, one can soon (for strong lines) verify the following relation $\beta_c \approx \beta\, W(r)/r$, which is accurate in the inner part of the wind ($v/v_\infty < 0.15$) and correct to within a factor of two in the outer region. Therefore the line net rate can be written as follows:

$$Z_{21} = \beta\left(1 - \frac{W(r)}{r}\frac{I_c}{S_{12}}\right). \tag{A5}$$

From Eq. (A3) it is easy to see that in order to get a depopulation of the ground level, the line net rate Z_{21} has to become negative, which is in fact true for our model. The reason for this behavior is the large ratio of I_c to the line source function in a region of the atmosphere where β and the dilution-factor $W(r)$ are not too small. Physically this can be understood by a temperature difference between the local electron temperature T_e, which determines the line source function, and the radiation temperature T_{rad} corresponding to I_c, which emerges from deep photospheric layers:

$$\frac{I_c}{S_{12}} = \frac{b_1}{b_2}\exp\left(\frac{h\nu_0}{k}(1/T_e - 1/T_{rad})\right). \tag{A6}$$

In the case of the line transition between level 1 and 2 ($\lambda_0 = 304$ Å) even a relative small temperature difference leads to a great effect, because the value of $h\nu_0/k \approx 4.7\ 10^5 \gg 1$.

In the following example (see Table A1) we have chosen three radius points in the atmosphere, to demonstrate the magnitude of I_c/S_{12} and Z_{12}. The values for b_1/b_2, β and the recombination rate R_{k1} are taken from the initial model without He II lines. The core intensity $I_c = 0.179\ 10^{-2}$ erg cm^{-2} s^{-1} Hz^{-1} ster^{-1} is equivalent to $T_{rad} \approx 5.3\ 10^4$ K.

The influence of the additional line term becomes obviously important above the sonic point due to the large variation of β in this region. From the last column of Table A1 one can see, that the departure coefficients would become negative in this region of the atmosphere if Eq. (A3) were used to calculate b_1 from the continuum model because:

$$\left|\left(\frac{n_2}{n_1}\right)^* \frac{A_{21} Z_{21}}{R_{k1}}\right| > 1 \quad (b_2 \text{ set to 1 for simplicity}).$$

At larger radii, the factor $W(r)/r$ decreases and the effect is diminished until finally Z_{21} becomes positive once again.

So far we have neglected the dependence on b_1 of the escape probability β, the ionisation rate R_{1k} and the line source function S_{12}, which makes our problem much more complicated. We have approximately

$\beta \approx 1/b_1$ for an optical thick line – the case we started from,

$R_{1k} \approx 1/b_1$ for $\tau_c \gg 1$, and $R_{1k} \approx \dfrac{1}{b_1(\tau_0)} W(r)$ for $\tau_c \ll 1$, where τ_0 is about 2/3.

Table A1. Radiative properties of the He II resonance line in the initial model

	$\frac{W(r)}{r}$	β	$\frac{I_c}{S_{12}}$	Z_{21}	$\left(\frac{n_2}{n_1}\right)^* \frac{A_{21}Z_{21}}{R_{k1}}$
1. Sonic point $r = 1.062\ R_*$ $T_e = 3.43\ 10^4$ K $v = 23.9$ km s^{-1}	0.31	$0.59\ 10^{-6}$	86	$-1.5\ 10^{-5}$	$-6.8\ 10^{-3}$
2. $\tau_{Ross} \approx -1.4$ $r = 1.4\ R_*$ $T_e = 3.33\ 10^4$ $v = 695$ km s^{-1}	0.11	$0.19\ 10^{-4}$	$2.5\ 10^3$	$-5.3\ 10^{-2}$	-28
3. $\tau_{Ross} \approx -2.7$ $r = 15.5\ R_*$ $T_e = 3.04\ 10^4$ $v = 2083$ km s^{-1}	$0.67\ 10^{-4}$	$0.70\ 10^{-3}$	$1.1\ 10^4$	$+1.9\ 10^{-4}$	$1.6\ 10^{-2}$

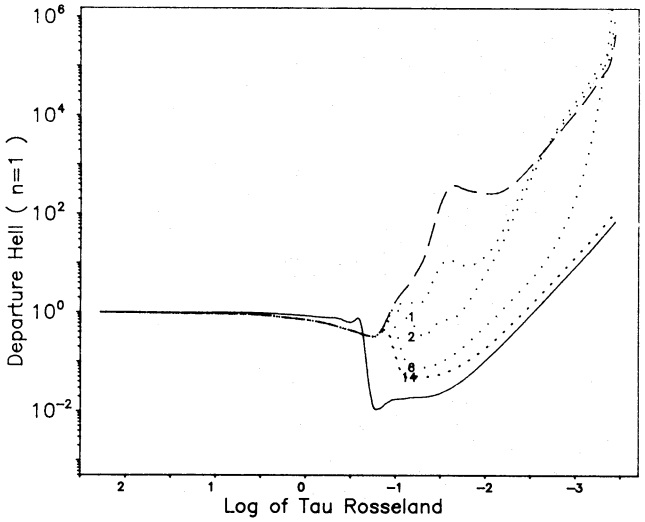

Fig. A2. Same as Fig. A1, but the dashed curve represents Eq. (A8) with β, β_c equal zero, whereas the dotted curves show the subsequent iterations of Eq. (A8)

If now b_1 becomes smaller and smaller, the values of β and R_{1k} increase steadily, which further enhances the effect of depopulation. Only the line source function (using $h\nu_0/kT \gg 1$)

$$S_{12} = \frac{2h\nu_0^3}{c^2}\frac{b_2}{b_1}\exp\left(\frac{-h\nu_0}{kT_e}\right) \tag{A7}$$

can put a limit to this development because as the source function increases the value of I_c/S_{12} becomes smaller. A new stable solution has to be found, which we have done iteratively in our simple analytical approach here.

We inserted (A7) directly into Eqs. (A3) and (A4) and solved again for b_1 to obtain

$$b_1 = \frac{R_{k1} + \left(\frac{n_2}{n_1}\right)^* \beta A_{21}\frac{R_{k2}}{R_{2k}+\beta A_{21}}}{R_{1k} + \left(\frac{n_2}{n_1}\right)^* \beta_c I_c A_{21}\frac{c^2}{2h\nu_0^3}\exp\left(\frac{h\nu_0}{kT_e}\right)\frac{R_{2k}}{R_{2k}+\beta A_{21}}}. \tag{A8}$$

Using the new value of b_1, β, β_c and the ionisation rate R_{1k} are recalculated and so on. All the other quantities $R_{k1}, R_{2k}, R_{k2}, I_c$ as well as the electron and He III density are regarded as constant during the iteration.

Figure A2 shows some of the iterations up to number 14. The first application of Eq. (A8) does not lead to a very large amount of depopulation but because of the change of β and R_{1k} described above the effect is enhanced and the region of depopulation spreads in both directions during the following iterations. Finally, the iterated application of Eq. (A8) comes close to the result of the numerical solution of the full problem described in Sect. 2.3. The remaining differences from the numerical solution are caused by the fact that only b_1, β_c, β and R_{1k} are iterated from the initial model while all other quantities are kept fixed.

References

Abbott, D.C.: 1982, *Astrophys. J.* **259**, 282
Abbott, D.C., Hummer, D.G.: 1985, *Astrophys. J.* **294**, 286
Aller, L.H.: 1948, *Astrophys. J.* **108**, 462
Aller, L.H., Wilson, O.C.: 1954, *Astrophys. J.* **119**, 243
Anderson, L.S.: 1985, *Astrophys. J.* **298**, 848
Auer, L.H.: 1971, *J. Quant. Spectros. Rad. Transf.* **11**, 573
Auer, L.H., Mihalas, D.: 1969, *Astrophys. J.* **158**, 641
Auer, L.H., Mihalas, D.: 1972, *Astrophys. J. Suppl.* **185**, 641
Bohannan, B., Abbott, D.C., Voels, S.A., Hummer, D.G.: 1986, *Astrophys. J.* **308**, 728
Cassinelli, J.P., Olson, G.L., Stalio, R.: 1978, *Astrophys. J.* **220**, 537
Castor, R.I., Simon, T.: 1983, *Astrophys. J.* **265**, 304
Clegg, R.E.S., Middlemass, D.: 1987, *Monthly Notices Roy. Astron. Soc.* **228**, 759
Drew, J.: 1988, preprint
Groenewegen, M.A.T., Lamers, H.J.G.L.M., Pauldrach, A.W.A.: 1989, preprint
Gruschinske, J., Kudritzki, R.P.: 1979, *Astron. Astrophys.* **77**, 341
Hamann, W.R.: 1980, *Astron. Astrophys.* **84**, 342
Hamann, W.R.: 1981a, *Astron. Astrophys.* **93**, 353
Hamann, W.R.: 1981b, *Astron. Astrophys.* **100**, 169

Hamann, W.R.: 1985, *Astron. Astrophys.* **148**, 364
Hamann, W.R.: 1986, *Astron. Astrophys.* **160**, 347
Heap, S.R., Torres, A.V.: 1988, Proc. IAU Symp. 131 *Planetary Nebulae*, ed. S. Torres-Peimbert, p. 308
Herrero, A.: 1987a, *Astron. Astrophys.* **171**, 189
Herrero, A.: 1987b, *Astron. Astrophys.* **186**, 231
Hillier, J.: 1987, *Astrophys. J. Suppl.* **63**, 947
Husfeld, D., Kudritzki, R.P., Simon, K.P., Clegg, R.E.S.: 1984, *Astron. Astrophys.* **134**, 139
Klein, R.J., Castor, J.I.: 1978, *Astrophys. J.* **220**, 902
Kudritzki, R.P.: 1973, *Astron. Astrophys.* **28**, 103
Kudritzki, R.P.: 1976, *Astron. Astrophys.* **52**, 11
Kudritzki, R.P.: 1979, Comm. of 22nd Intern. Liege Astrophys. Coll., p. 295
Kudritzki, R.P.: 1980, *Astron. Astrophys.* **85**, 174
Kudritzki, R.P.: 1988, Proc. IAU Coll. 95 *Faint Blue Stars*, ed. Davis Philip, p. 177
Kudritzki, R.P., Simon, K.P.: 1978, *Astron. Astrophys.* **70**, 653
Kudritzki, R.P., Simon, K.P., Hamann, W.R.: 1983, *Astron. Astrophys.* **118**, 245
Kudritzki, R.P., Hummer, D.G.: 1986, Proc. IAU Symp. 116 *Luminous Stars and Associations in Galaxies*, eds. De Loore et al., p. 3
Kudritzki, R.P., Pauldrach, A., Puls, J.: 1987, *Astron. Astrophys.* **173**, 293
Kudritzki, R.P., Méndez, R.H.: 1988, Proc. IAU Symp. 131 *Planetary Nebulae*, ed. S. Torres-Peimbert, p. 273
Lamers, H.J.G.L.M., Morton, D.: 1976, *Astrophys. J. Suppl.* **32**, 715
Lamers, H.J.G.L., Waters, L.B.F.M.: 1984, *Astron. Astrophys.* **136**, 37
Lamers, H.J.G.L.M., Waters, L.B., Wesselius, P.R.: 1984, *Astron. Astrophys.* **134**, L17
Leitherer, C.: 1988, *Astrophys. J.* **326**, 356
Lucy, L.B.: 1982, *Astrophys. J.* **255**, 286
Méndez, R.H., Kudritzki, R.P., Herrero, A., Husfeld, D., Groth, H.G.: 1988, *Astron. Astrophys.* **190**, 113
Mihalas, D.: 1972, *Non-LTE Model Atmospheres for B and O stars*, NCAR-TN/STR-76
Mihalas, D., Hummer, D.G.: 1974, *Astrophys. J. Suppl.* **265**, 343
Mihalas, D., Kunasz, P., Hummer, D.G.: 1975, *Astrophys. J.* **202**, 465
Morton, D.C., Wright, A.E.: 1978, *Monthly Notices Roy. Astron. Soc.* **182**, 479
Olson, G.L., Ebbets, D.: 1981, *Astrophys. J.* **248**, 1021
Olson, G.L., Auer, L.M., Buchler, J.R.: 1986, *J. Quant. Spectrosc. Radiat. Transfer* **35**, 431
Owocki, S.P., Castor, J.I., Rybicki, G.B.: 1988, *Astrophys. J.* **335**, 914
Panagia, N., Felli, M.: 1975, *Astron. Astrophys.* **39**, 1
Pauldrach, A.: 1987a, Thesis, Ludwig-Maximilians-Universität, München
Pauldrach, A.: 1987b, *Astron. Astrophys.* **183**, 295
Pauldrach, A., Puls, J., Kudritzki, R.P.: 1986, *Astron. Astrophys.* **164**, 86
Pauldrach, A., Herrero, A.: 1988, *Astron. Astrophys.* **199**, 262
Puls, J.: 1987a, Thesis, Ludwig-Maximilians-Universität, München
Puls, J.: 1987b, *Astron. Astrophys.* **184**, 227
Puls, J., Herrero, A.: 1988, *Astron. Astrophys.* **204**, 219
Schönberner, D.: 1983, *Astrophys. J.* **272**, 708
Schöning, T., Butler, K.: 1989a, *Astron. Astrophys.* **219**, 326
Schöning, T., Butler, K.: 1989b, *Astron. Astrophys. Suppl.* **78**, 51
Simon, K.P., Jonas, G., Kudritzki, R.P., Rahe, J.: 1983, *Astron. Astrophys.* **125**, 34
Schönberner, D.: 1983, *Astrophys. J.* **272**, 708
Vidal, C.R., Cooper, J., Smith, E.W.: 1973, *Astrophys. J. Suppl.* **25**, 37
Werner, K.: 1987, Thesis, Christian Albrecht Universität, Kiel
Werner, K.: 1988, *Astron. Astrophys.* **204**, 159
Werner, K., Husfeld, D.: 1985, *Astron. Astrophys.* **148**, 417
Wood, P.R., Faulkner, D.J.: 1986, *Astrophys. J.* **307**, 659
Wright, A.E., Barlow, M.J.: 1975, *Monthly Notices Roy Astron. Soc.* **170**, 41